International Journal of Mechanical Sciences 224 (2022) 107280

Contents lists available at ScienceDirect

International Journal of Mechanical Sciences

journal homepage: www.elsevier.com/locate/ijmecsci

Design of tunable hierarchical waveguides based on Fibonacci-like microstructure

Andrea Bacigalupo [a,1], Maria Laura De Bellis [b,*,1], Marcello Vasta [b,1]

[a] University of Genoa, Department DICCA, via Montallegro 1, Genoa, Italy
[b] University of Chieti-Pescara, Department INGEO, Viale Pindaro 42, Pescara, Italy

ARTICLE INFO

Keywords:
Waveguiding
Quasi-periodic metamaterial
Fibonacci-like superlattice
Piezoelectric shunting
Bloch wave propagation

ABSTRACT

A novel class of Fibonacci-based high performance tunable hierarchical waveguides is here proposed and special focus is devoted to the design of adaptive-passive control systems for the Bloch wave propagation. By exploiting the features of periodic approximants, the metamaterial is conceived by the proper repetition of an elementary cell along a fixed direction. This elementary cell is made up of two building blocks repeated according to the Fibonacci sequence, to form a quasi-periodic finite microstructured system The former building block is made of a homogeneous elastic material, while the latter is a microstructured two-phase laminate. One of these phases is piezoelectric shunted by a suitably conceived electrical circuit, such that the constitutive properties of the piezoelectric phase are tuned by adjusting its equivalent impedance/admittance. Moreover, the overall constitutive properties of the microstructured layer are determined, exploiting the scale separation, via an asymptotic homogenization scheme. Then, it is possible to determine the frequency band structure of the tunable waveguide by exploiting the transfer matrix approach. With the aim of providing broad design directions, attention is paid to characterizing the dispersion waves properties of the tunable Fibonacci-like superlattices described by several generations of the Fibonacci sequence and for different values of the orientation angle of the two-phase laminate.

1. Introduction

Recent advances in the field of metamaterials, both concerning theoretical studies and technological solutions, are paving the way for appealing applications including waveguiding, focusing, band gaps control, collimation and wave polarization [1–20]. In this context acoustic metamaterials are in general designed from phononic crystals, enriched by local resonators, giving rise to special sub-wavelength properties. Due to the high flexibility in tailoring their microscopical architecture, it is possible to obtain extreme macroscopic properties, well beyond those of the corresponding base materials [21–34]. In particular, remarkable effort has been devoted to the optimal design of metamaterials, exploiting parametric and topological optimization techniques [35–43]. The challenging objective of wave propagation control can also be achieved through avant-garde techniques involving the use of active phases that exploit multi-field couplings. The key point of these approaches is the intriguing possibility of designing novel metamaterials with tunable constitutive properties without varying their mass. Specifically, a successful solution consists in conceiving heterogeneous periodic devices that include shunted piezoelectric phases, i.e. piezoelectric materials coupled in parallel to suitable electrical circuits, in both active and passive control schemes. These design strategies are effectively exploited to realize high-performance waveguides and/or acoustic metafilters [44–55]. Most design approaches and manufacturing methods have been based so far on periodic tessellations of unit cells in one, two or three dimensions.

On the other hand, quasi-periodic metamaterials, characterized by non periodic but ordered tessellations, have hardly been researched, although the peculiar optical behavior of quasi-crystals, recently discovered in [56], seems to suggest a promising potential in the design of devices with unprecedented global physical properties, for several applications in different engineering fields. Quasi-crystals exhibit microstructures that, in a sense, are intermediate between the periodic crystals and the amorphous ones. In particular, on the one hand crystals are characterized by optical diffraction figures exhibiting infinitely countable and well-defined peaks, together with long-range order and translational symmetry. This is not the case of amorphous materials. On the other hand, quasi-periodic quasi-crystals keep showing diffraction figures with infinitely countable and well-defined peaks, as well

* Corresponding author.
E-mail address: marialaura.debellis@unich.it (M.L. De Bellis).
[1] All authors listed have made a substantial, direct and intellectual contribution to the work, and approved it for publication.

https://doi.org/10.1016/j.ijmecsci.2022.107280
Received 14 January 2022; Received in revised form 28 March 2022; Accepted 9 April 2022
Available online 23 April 2022

as long-range order, as crystals, but lack translational symmetry, as amorphous materials. It is noticeably observed that quasi-crystals show icosahedral symmetry, not achievable in periodic crystals structures due to the crystallographic restriction theorem.

Quasi-periodic metamaterials are artificial materials made-up from the regular but not periodic repetition of two or more either homogeneous (one-phase) or microstructured (multi-phase) building blocks, resulting into a ordered tessellation having *long-range order* at the macroscopic scale and *short-range order* at the microscopic one. These tilings can be obtained in different ways, as for example, aperiodic microstructures inspired by Voronoi decomposition [57], Pendrose tilings [58], but also further aperiodically ordered structures obtained via the so-called inflation (or deflation) procedure, or via projection from higher-dimensional periodic lattices [59]. One more example of quasi-periodic composites is given by building blocks, of different kind ranging from one-phase lattice type up to multi-phase composites, that repeat themselves along one or more directions in accordance with the recursive sequence of (generalized) Fibonacci numbers sequence [60], as well as the Thue–Morse sequence [61], and the Cantor sequence [62], resulting in the so-called (generalized) Fibonacci-like, Thue–Morse-like and Cantor-like superlattices, among others.

The study of wave propagation in infinite mechanical systems with quasi-periodic topology is often performed resorting to the so-called periodic approximants [63]. In this context, a quasi-periodic material can be obtained from the periodic repetition, along appropriate periodicity directions, of an elementary cell consisting of building blocks that repeat themselves to form a finite system with a quasi-periodic microstructure. As the size of the elementary cell increases, corresponding to a larger portion of the quasi-crystalline material, an increasingly accurate characterization of the dispersion properties of the quasi-periodic metamaterial is obtained. In other terms, a single portion of the quasicrystal, periodically repeated, can be considered suitable to represent the whole infinite structure. Focusing the attention on quasi-periodic mechanical superlattices, to date few examples have been proposed in literature, with the aim of designing materials with extreme stiffness and strength as well as for applications devoted to waveguiding, wave manipulation, filtering among others [64–71], and still open issues remain to investigate.

Within this scientific framework, we propose novel hierarchical waveguides, combining possible advantages of Fibonacci based microstrustures and tunable metamaterials, for the adaptive-passive wave propagation control. The key idea is exploiting the features of periodic approximants to design a new class of nested Fibonacci-like superlattices obtained by the suitable repetition of an elementary cell along a fixed direction. More specifically the elementary cell is made up of two building blocks that repeat themselves, according to the Fibonacci sequence, to form a finite system with a quasi-periodic microstructure. Specifically, one building block is made of a homogeneous elastic material, while the second is a microstructured two-phase laminate, with characteristic size much smaller than that of the corresponding building block (scale separation assumption). The microstructured laminate encompasses a piezoelectric phase shunted by a properly conceived electrical circuit [53]. Therefore the equivalent impedance/admittance of the electrical circuit can be adjusted in order to tweak the constitutive properties of the shunting piezoelectric phase. It follows that the constitutive properties of the shunted piezoelectric phase can be fully adjusted by modifying a tuning parameter governing the properties of the electrical circuit. By exploiting the scale separation, a first order asymptotic homogenization scheme is first applied to grasp the overall constitutive properties of the microstructured building block, that in turn depends on the tuning parameter. The transfer matrix approach is then used to determine the dispersion properties of the waveguides, associated both to different generations of the Fibonacci sequence and to different values of the orientation angle of the layered two-phase composite that make up the microstructured building block. A critical investigation of the Fibonacci based hierarchical waveguide behavior is performed as the tuning parameter changes aimed at providing broad guidance to inspire optimal design solutions.

The layout of the paper is as follows. In Section 2 the proposed Fibonacci based hierarchical waveguide is described. Section 3 is devoted to derive the overall constitutive properties of the microstructured building block via a first order asymptotic homogenization scheme. In Section 4 the field equations governing the in-plane free Bloch wave propagation within the hierarchical waveguide are derived and the frequency band structure is obtained using the transfer matrix approach. In Section 5 numerical experiments are useful both to investigate the performances of the waveguide for different generations of the Fibonacci sequence, and to validate the performances of the pass and stop bands tunable control of the hierarchical Fibonacci-like metamaterial. Finally, concluding remarks are discussed in Section 6.

2. Fibonacci based hierarchical waveguide

We want to design a particular waveguide with hierarchical structure, obtained by the proper repetition of an elementary cell along a periodicity vector, resulting in a composite laminate. The elementary cell is made up of two (possibly microstructured) materials, in the following referred to as *building block* A and B, which repeat themselves according to the well-known Fibonacci sequence, fulfilling the following concatenation recursive rule $S_j = S_{j-1}S_{j-2}$ $(j \geq 2)$ starting with $S_0 = A$ and $S_1 = B$. The number of building blocks that form the S_j is equal to $n_j = n_{j-1} + n_{j-2}\,(j \geq 2, n_0 = n_1 = 1)$, with $\lim_{j\to\infty} \frac{n_{j+1}}{n_j} = \phi$, being $\phi = (\sqrt{5}+1)/2$ the so-called *golden mean*. In this way Fibonacci generations are S_2 = BA, S_3 = BAB, S_4 = BABBA, S_5 = BABBABAB, S_6 = BABBABBABAB, S_7 = BABBABABBABABABBABAB and so on, as schematically shown in Fig. 1 where the specific elementary cell $\mathfrak{A}^{S_n}$ is highlighted using bright colors and capital letters to denote building blocks. For illustrative purposes, a 2D-view of the elementary cell $\mathfrak{A}^{S_3}$ associated with the Fibonacci generation S_3 at the macroscopic scale is shown in Fig. 2(a). The cell has out-of-plane thickness w, the layer B of thickness d_B is made of a homogeneous material, while the layer A, of thickness d_A, is made of a laminated microstructured material consisting, in turn, of two phases A_1 and A_2, of thickness d_{A1} and d_{A2}, respectively, where the orientation of layers, identified by the unit vector $\mathbf{a}_1$, can generally be inclined by the *orientation angle* θ with respect to the layer B, identified by the unit vector $\mathbf{e}_1$, see Fig. 2(b). Finally, Fig. 2(c) illustrates in detail the periodic cell $\mathfrak{A}$ of the microstructured building block A, characterized only by the periodicity vector $\mathbf{v} = \mathrm{v}_2\mathbf{a}_2 = (d_{A1} + d_{A2})\,\mathbf{a}_2$ given the translational invariance along $\mathbf{a}_1$.

Regarding the constitutive behavior of materials, we assume that the building block B is made of a soft and light linear elastic isotropic material, while the A_1 layer is made of a rigid and heavy linear isotropic elastic material and the A_2 layer is made of a linear shunted piezoelectric material. Each piezoelectric layer, polarized along the out-of-plane direction, is coupled to an external electric circuit with tunable impedance/admittance, as schematically shown in Fig. 3(a). It follows that, the constitutive properties of the piezoelectric shunting can be tuned by adjusting the characteristic properties of the passive bipole to obtain a proper control of the spectral properties of the hierarchical waveguide. By exploiting the scale separation in the building block A, i.e. that $d_{A1} + d_{A2} \ll d_A$, we can determine its first order homogenized response by applying an asymptotic homogenization scheme, as explained in Section 3. Subsequently, in Section 4 we will study in detail the band structure of the tunable hierarchical metamaterial consisting of the building block B and a homogenized material, equivalent to the microstructured building block A, in the so-called *high fidelity frequency range*. This range is defined as the frequency range in which the Floquet–Bloch spectra, obtained both considering the building block A as homogenized and that considering the building block A as microstructured, are in excellent agreement. It is important to note that

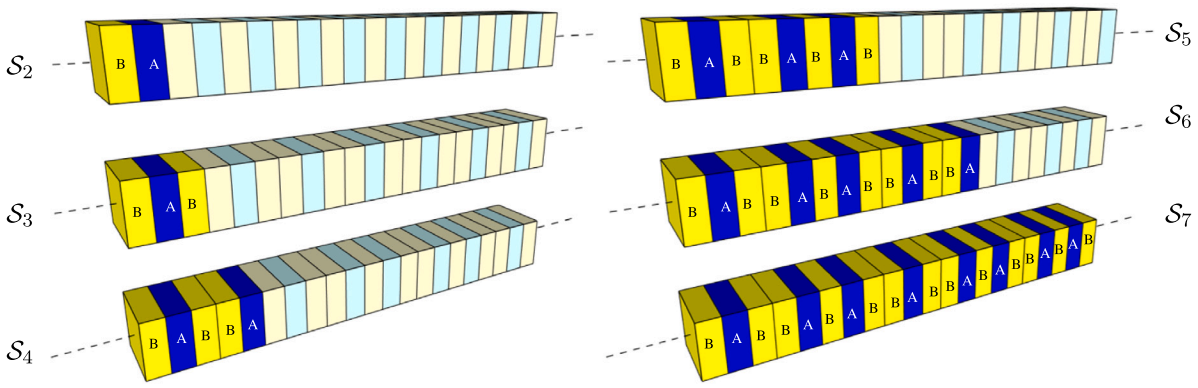

Fig. 1. Fibonacci generations of the hierarchical composite material made up of building blocks A and B. Each generation $\mathcal{S}_2$, $\mathcal{S}_3$, $\mathcal{S}_4$, $\mathcal{S}_5$, $\mathcal{S}_6$, $\mathcal{S}_7$ is repeated periodically along the periodicity vector.

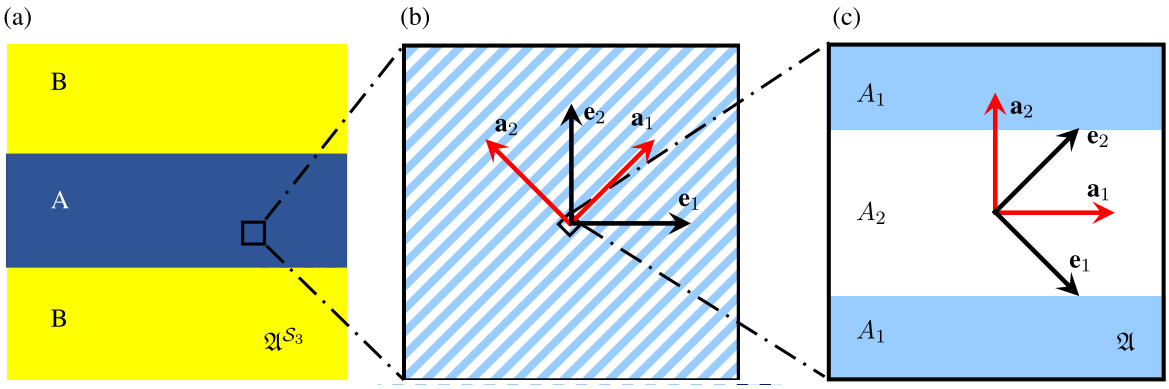

Fig. 2. (a) 2D view of the elementary cell $\mathfrak{A}^{\mathcal{S}_3}$ corresponding to the Fibonacci generation $\mathcal{S}_3$ at the macroscopic scale; (b) zoomed view of the microstructured building block A made of a layered composite with local $\{\mathbf{a}_1, \mathbf{a}_2\}$ and global $\{\mathbf{e}_1, \mathbf{e}_2\}$ orthonormal bases at the microscopic scale; (c) zoomed view of the periodic cell $\mathfrak{A}$ embedded in the microstructured building block A.

this range tends to grow as the separation of scales increases. the band structure of the tunable hierarchical metamaterial consisting of the building block B and a homogenized material, equivalent to the microstructured building block A, in the so-called *high fidelity frequency range*. This range is defined as the frequency range in which the Floquet–Bloch spectra, obtained both considering the building block A as homogenized and that considering the building block A as microstructured, are in excellent agreement. It is important to note that this range tends to grow as the separation of scales increases.

3. Asymptotic homogenization of the layered material

Let us now consider the microstructured building block A, made of the repetition of the periodic cell $\mathfrak{A}$ (in Fig. 2(c)) along its periodicity vector $\mathbf{v}$. The in-plane governing equations are expressed in component form with respect to the basis $\{\mathbf{a}_1, \mathbf{a}_2\}$, and in the transformed Laplace space, as follows

$$\left(\mathsf{C}^m_{ijhl}(s)\hat{\mathsf{u}}_{h,l}\right)_{,j} + \hat{\mathsf{b}}_i = \rho^m s^2 \hat{\mathsf{u}}_i, \tag{1}$$

where $\mathsf{C}^m_{ijhl}(s)$ are the constitutive tensor components, s is the complex Laplace variable, $\hat{\mathsf{u}}_i$ are the in-plane transformed displacement components, $\hat{\mathsf{b}}_i$ the transformed source term components, ρ^m is the mass density and the comma denotes the generalized partial derivative with respect to x_j, i.e. the components of the in-plane position vector $\mathbf{x} = \mathsf{x}_j \mathbf{a}_j \in \mathbb{R}^2$, with $i, j, h, l = 1, 2$. Due to the periodic repetition of layers A_1 and A_2, both the constitutive tensor and the mass density are $\mathfrak{A}$-periodic and satisfy translation invariance with respect to $\mathbf{a}_1$ thus being x_1-independent, so that

$$\mathsf{C}^m_{ijhl}\left(\mathsf{x}_2\,\mathbf{a}_2 + n\mathbf{v}, s\right) = \mathsf{C}^m_{ijhl}\left(\mathsf{x}_2\,\mathbf{a}_2, s\right),$$

$$\rho^m\left(\mathsf{x}_2\,\mathbf{a}_2 + n\mathbf{v}, s\right) = \rho^m\left(\mathsf{x}_2\,\mathbf{a}_2\right), \qquad \forall \mathsf{x}_2\,\mathbf{a}_2 \in \mathfrak{A}, \tag{2}$$

where $n \in \mathbb{Z}$ and $\mathbf{v} = \mathsf{v}_2\,\mathbf{a}_2$ is the periodicity vector. Note that the components C^m_{ijhl} of the linear elastic phase A_1 are s-independent, while those of the shunting piezoelectric phase A_2, polarized along the out-of-plane direction and denoted with the apex SA_2, are in general s-dependent and, accordingly with [53], take the following form

$$\mathsf{C}^{SA_2}_{ijhl}(\lambda(s)) = \mathsf{C}^{A_2}_{ijhl} + \frac{\mathsf{e}^{A_2}_{ij3}\widetilde{\mathsf{e}}^{A_2}_{3hl}}{\beta^{SA_2}_{33}(\lambda(s))} - \left(\mathsf{C}^{A_2}_{ij33} + \frac{\mathsf{e}^{A_2}_{ij3}\widetilde{\mathsf{e}}^{A_2}_{333}}{\beta^{SA_2}_{33}(\lambda(s))}\right)\left(\frac{\mathsf{C}^{A_2}_{33hk} + \frac{\mathsf{e}^{A_2}_{333}\widetilde{\mathsf{e}}^{A_2}_{3hl}}{\beta^{SA_2}_{33}(\lambda(s))}}{\mathsf{C}^{A_2}_{3333} + \frac{\mathsf{e}^{A_2}_{333}\widetilde{\mathsf{e}}^{A_2}_{333}}{\beta^{SA_2}_{33}(\lambda(s))}}\right), \tag{3}$$

where $\mathsf{C}^{A_2}_{ijhl}$ are the components of the fourth order elasticity tensor, $\mathsf{e}^{A_2}_{ij3}$ are the components of the third order stress-charge coupling tensor of the piezoelectric material and $\widetilde{\mathsf{e}}^{A_2}_{pqs} = \mathsf{e}^{A_2}_{qsp}$ its transpose. Moreover, the auxiliary s-dependent function $\beta^{SA_2}_{33}(s) = \beta^{A_2}_{33}(1 + \lambda(s))$ is introduced, being $\beta^{A_2}_{33}$ the component of the second order permittivity tensor and being $\lambda(s) = L^{A_2} Y^S_{33}(s)/(s\,\beta^{A_2}_{33}\,\Delta^{A_2})$ the so-called *tuning function* with linear dependence on the generic equivalent shunting admittance $Y^S_{33}(s)$, which is expressed in terms of one or more tuning parameters defining the properties of the electrical circuit at hand. Note that Δ^{A_2} is the in-plane area of the piezoelectric layer A_2, and $L^{A_2} = w$. It is worth-noting that the constitutive relation of the shunted piezoelectric material, in Eq. (3), is obtained from an in-plane condensation of those associated to a three-dimensional orthotropic piezoelectric material with polarization along the out-of-plane direction. It results in-plane uncoupled constitutive equations, formally equivalent to the equations of a linearly elastic dielectric material [72]. It follows that the components of the equivalent constitutive tensor related to the

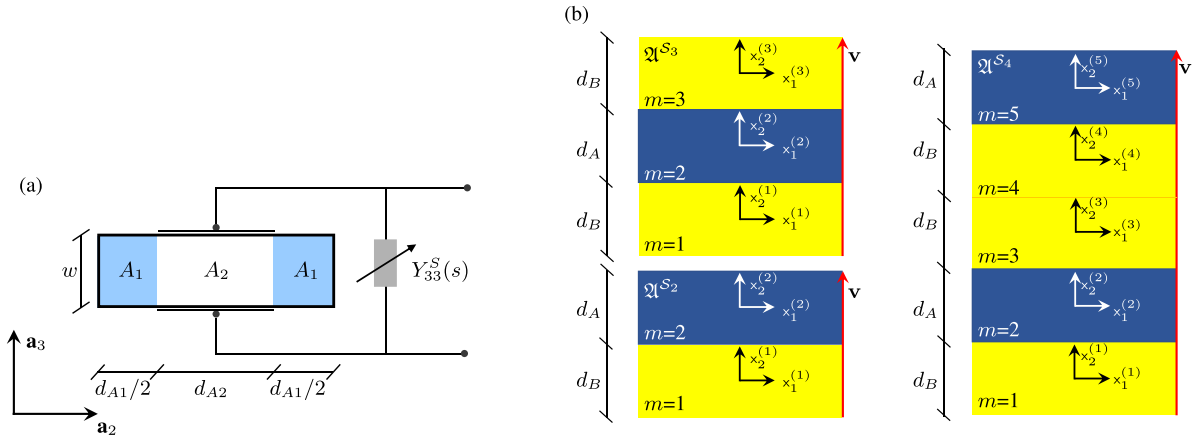

Fig. 3. (a) Scheme of the elementary cell in the building block A containing the shunted piezoelectric material; (b) Periodic cells for generations $\mathcal{S}_2$, $\mathcal{S}_3$ and $\mathcal{S}_4$ together with local coordinate systems along each layer.

$$
\begin{aligned}
\mathsf{C}^{A}_{1111}(s) &= \frac{\zeta^2\mathsf{C}^{A_1}_{1111}\mathsf{C}^{SA_2}_{2222}+\zeta(\mathsf{C}^{SA_2}_{1111}\mathsf{C}^{SA_2}_{2222}-(\mathsf{C}^{A_1}_{1122})^2+2\mathsf{C}^{A_1}_{1122}\mathsf{C}^{SA_2}_{1122}-(\mathsf{C}^{SA_2}_{1122})^2+\mathsf{C}^{A_1}_{1111}\mathsf{C}^{A_1}_{2222})+\mathsf{C}^{SA_2}_{1111}\mathsf{C}^{A_1}_{2222}}{(\zeta+1)(\mathsf{C}^{A_1}_{2222}+\zeta\mathsf{C}^{SA_2}_{2222})},\\
\mathsf{C}^{A}_{2222}(s) &= \frac{(\zeta+1)\mathsf{C}^{A_1}_{2222}\mathsf{C}^{SA_2}_{2222}}{\mathsf{C}^{A_1}_{2222}+\zeta\mathsf{C}^{SA_2}_{2222}},\\
\mathsf{C}^{A}_{1212}(s) &= \frac{(\zeta+1)\mathsf{C}^{A_1}_{1212}\mathsf{C}^{SA_2}_{1212}}{\mathsf{C}^{A_1}_{1212}+\zeta\mathsf{C}^{SA_2}_{1212}},\\
\mathsf{C}^{A}_{1122}(s) &= \frac{\mathsf{C}^{SA_2}_{1122}\mathsf{C}^{A_1}_{2222}+\zeta\mathsf{C}^{A_1}_{1122}\mathsf{C}^{SA_2}_{2222}}{\mathsf{C}^{A_1}_{2222}+\zeta\mathsf{C}^{SA_2}_{2222}},\\
\rho^{A} &= \frac{\rho^{A_1}\zeta+\rho^{A_2}}{1+\zeta},
\end{aligned}
\tag{4}
$$

Box I.

shunted piezoelectric material only depend on the constitutive tensor components of the piezoelectric phase and on the electrical circuit admittance.

By exploiting the asymptotic homogenization scheme, consistently with [73,74], the overall s-dependent first order constitutive tensor components of the microstructured building block A together with the overall mass density are determined and result as given in Box I. where $\zeta = d^{A1}/d^{A2}$ and the apex A_i refers to ith of the two layers. It is important to underline that the s-dependent perturbation functions involved in the determination of overall properties are x_1-independent and therefore they depend exclusively on the geometric ratio ζ. Changing from the orthonormal basis $\{\mathbf{a}_1, \mathbf{a}_2\}$ to the basis $\{\mathbf{e}_1, \mathbf{e}_2\}$, see Fig. 2(b), the components of the transformed constitutive tensor vary accordingly with the transformation law $C^{A}_{i_1j_1h_1k_1} = \mathsf{C}^{A}_{ijhk}Q_{ii_1}Q_{jj_1}Q_{hh_1}Q_{kk_1}$, where the rotation tensor components are $Q_{11} = \cos(\theta)$, $Q_{12} = \sin(\theta)$, $Q_{21} = -\sin(\theta)$, $Q_{22} = \cos(\theta)$ and the angle θ is positive if the rotation is clockwise. Specifically, the s-dependent overall elastic tensor components in the basis $\{\mathbf{e}_1, \mathbf{e}_2\}$ become

$$
\begin{aligned}
C^{A}_{1111}(s) &= \mathsf{C}^{A}_{1111}\cos^4(\theta)+\left(2\mathsf{C}^{A}_{1122}+4\mathsf{C}^{A}_{1212}\right)\cos^2(\theta)\sin^2(\theta)+\mathsf{C}^{A}_{2222}\sin^4(\theta),\\
C^{A}_{2222(s)} &= \mathsf{C}^{A}_{2222}\cos^4(\theta)+\left(2\mathsf{C}^{A}_{1122}+4\mathsf{C}^{A}_{1212}\right)\cos^2(\theta)\sin^2(\theta)+\mathsf{C}^{A}_{1111}\sin^4(\theta),\\
C^{A}_{1212}(s) &= \left(\mathsf{C}^{A}_{1111}-2\mathsf{C}^{A}_{1122}+\mathsf{C}^{A}_{2222}\right)\cos^2(\theta)\sin^2(\theta)+\mathsf{C}^{A}_{1212}\cos^2(2\theta),\\
C^{A}_{1122}(s) &= \left(\mathsf{C}^{A}_{1111}-4\mathsf{C}^{A}_{1212}+\mathsf{C}^{A}_{2222}\right)\cos^2(\theta)\sin^2(\theta)\\
&\quad+\mathsf{C}^{A}_{1122}\left[\cos^4(\theta)+\sin^4(\theta)\right],\\
C^{A}_{1112}(s) &= \mathsf{C}^{A}_{1111}\cos^3(\theta)\sin(\theta)-\frac{1}{4}\left(\mathsf{C}^{A}_{1122}+2\mathsf{C}^{A}_{1212}\right)\sin(4\theta)\\
&\quad-\mathsf{C}^{A}_{2222}\sin^3(\theta)\cos(\theta),\\
C^{A}_{2212}(s) &= \mathsf{C}^{A}_{1111}\cos(\theta)\sin^3(\theta)+\frac{1}{4}\left(\mathsf{C}^{A}_{1122}+2\mathsf{C}^{A}_{1212}\right)\sin(4\theta)\\
&\quad-\mathsf{C}^{A}_{2222}\sin(\theta)\cos^3(\theta).
\end{aligned}
\tag{5}
$$

Note that in the particular case of significant technological interest, in which the equivalent electrical circuit is characterized by a purely capacitive admittance $Y^S_{33}(s) = sC$, the tuning function turns out to be s-independent, i.e. $\lambda = CL^{A_2}/(\beta^{A_2}_{33}A^{A_2})$, as well as the constitutive tensor components $\mathsf{C}^{SA_2}_{ijkl}$. In this case, the complex frequency s is purely imaginary, i.e. $s = \imath\omega$, being $\imath$ the imaginary unit and $\omega \in \mathbb{R}$ the angular frequency of Bloch waves. It is also noted that, considering a shunted orthotropic piezoelectric material polarized along the out of plane direction, the constitutive tensor components $\mathsf{C}^{SA_2}_{\alpha\alpha\beta\beta}$ $(\alpha, \beta = 1, 2)$ turns out to be a function of the tuning variable λ and has vertical asymptotes for the *resonance* value of the tuning parameter $\lambda_R = -\left(1+e^{A_2}_{333}\tilde{e}^{A_2}_{3hl}/\left(C^{A_2}_{3333}\beta^{A_2}_{33}\right)\right)$, see [53] for a detailed description of the peculiar constitutive behavior of the shunting phase. Note that the case with $\lambda = 0$ corresponds to a non shunted piezoelectric material, i.e. to the case of open circuit or of standard piezoelectric material.

4. Acoustic dispersion properties of the waveguide

We are herein interested in investigating the free wave propagation in the hierarchical microstructured waveguide considering an equivalent electrical circuit characterized by a purely capacitive admittance.

To this aim, we define the in-plane governing equations in component form with respect to the basis $\{\mathbf{e}_1, \mathbf{e}_2\}$, and in the frequency domain at the macroscopic scale

$$\left(C^M_{ijhl}\hat{u}_{h,l}\right)_{,j} + \rho^M\omega^2\hat{u}_i = 0, \tag{6}$$

where C^M_{ijhl} are the constitutive tensor components, ρ^M is the mass density. Note that the components C^M_{ijhl} are $\mathfrak{A}^{S_n}$-periodic and satisfy the translation invariance along the layering direction. According to the Floquet–Bloch theory, the solution of field equations in a quasi-periodic waveguide can be written, by exploiting the so-called Bloch decomposition, as

$$\hat{\mathbf{u}}(x_1, x_2, \omega) = \hat{\mathbf{w}}(x_2, \omega)e^{\imath\mathbf{k}\cdot\mathbf{x}}, \tag{7}$$

where the vector $\hat{\mathbf{w}}(x_2, \omega) = \hat{w}_i(x_2, \omega)\mathbf{e}_i$ collects the Bloch amplitudes that are $\mathfrak{A}^{S_n}$-periodic and satisfy the translation invariance along $\mathbf{e}_1$. Moreover $\mathbf{k} = k_i\mathbf{e}_i$ is the wave vector. By plugging Eqs. (7) in (6) we obtain

$$\begin{aligned}&\left(C^M_{i2h2}\hat{w}_{h,2}\right)_{,2} + \imath k_j\left[(C^M_{ijh2} + C^M_{i2hj})\hat{w}_{h,2} + C^M_{i2hj,2}\hat{w}_h\right]\\ &\quad - (C^M_{ijhk}k_k k_j - \rho^M\omega^2\delta_{ih})\hat{w}_h = 0.\end{aligned} \tag{8}$$

Focusing the attention on a single layer Γ (with Γ=A,B) the following system of second order ordinary differential equations in the x_2-variable is obtained

$$C^\Gamma_{i2h2}\hat{w}_{h,22} + \imath k_j(C^\Gamma_{ijh2} + C^\Gamma_{i2hj})\hat{w}_{h,2} - (C^\Gamma_{ijhk}k_k k_j - \rho^\Gamma\omega^2\delta_{ih})\hat{w}_h = 0. \tag{9}$$

By switching to the operatorial form, Eq. (9) becomes

$$\mathbf{C}_2\hat{\mathbf{w}}'' + \mathbf{C}_1\hat{\mathbf{w}}' + \mathbf{C}_0\hat{\mathbf{w}} = \mathbf{0}, \tag{10}$$

where apex $'$ denotes the x_2- derivative and $\mathbf{C}_2$, $\mathbf{C}_1$ and $\mathbf{C}_0$ are 2×2 matrices collecting the coefficients of the field equation. By introducing the 4-component vector $\hat{\mathbf{v}} = (\hat{\mathbf{w}}'\ \hat{\mathbf{w}})^T$ in the state space, the following equivalent system of first order differential equations, governed by two 4×4 coefficient block matrices, is obtained

$$\begin{bmatrix}\mathbf{C}_2 & \mathbf{0}\\ \mathbf{0} & \mathbf{I}\end{bmatrix}\hat{\mathbf{v}}' + \begin{bmatrix}\mathbf{C}_1 & \mathbf{C}_0\\ -\mathbf{I} & \mathbf{0}\end{bmatrix}\hat{\mathbf{v}} = \mathbf{D}_1\hat{\mathbf{v}}' + \mathbf{D}_0\hat{\mathbf{v}} = \mathbf{0}. \tag{11}$$

The general solution of the first order ordinary differential system (11) can be written, by invoking the matrix exponential formalism, as

$$\hat{\mathbf{v}} = e^{-\mathbf{D}_1^{-1}\mathbf{D}_0 x_2}\mathbf{c}, \tag{12}$$

defined except for the vector of constants $\mathbf{c}$. Similarly the traction vector $\hat{\mathbf{s}}$ is defined

$$\hat{\mathbf{s}}(x_1, x_2, \omega) = \hat{\mathbf{t}}(x_2, \omega)e^{\imath\mathbf{k}\cdot\mathbf{x}}, \tag{13}$$

as a function of the vector $\hat{\mathbf{t}}$ collecting the relevant stress tensor components

$$\hat{\mathbf{t}}(x_2, \omega) = (\hat{\sigma}_{21}\ \ \hat{\sigma}_{22})^T, \tag{14}$$

where the apex T denotes the transpose. It is useful to define the following block vector collecting the Bloch amplitudes and the tractions

$$\hat{\mathbf{y}}(x_1, x_2, \omega) = \begin{bmatrix}\hat{\mathbf{w}}(x_1, x_2, \omega)\\ \hat{\mathbf{s}}(x_1, x_2, \omega)\end{bmatrix} = e^{\imath\mathbf{k}\cdot\mathbf{x}}\begin{bmatrix}\mathbf{0} & \mathbf{I}\\ \mathbf{C}_2 & \imath\mathbf{C}_2 k_2\end{bmatrix}\hat{\mathbf{v}}(x_1, x_2, \omega), \tag{15}$$

and by plugging (12) in (15), the compact form of the solution is obtained as

$$\hat{\mathbf{y}}(x_1, x_2, \omega) = e^{\imath\mathbf{k}\cdot\mathbf{x}}\begin{bmatrix}\mathbf{0} & \mathbf{I}\\ \mathbf{C}_2 & \imath\mathbf{C}_2 k_2\end{bmatrix}e^{-\mathbf{D}_1^{-1}\mathbf{D}_0 x_2}\mathbf{c}. \tag{16}$$

Let us consider the single mth layer, pertaining to the elementary cell shown in Fig. 3(b) for generations S_2, S_3 and S_4, respectively, having thickness d_m. A proper local coordinate system is herein defined, in which x_1 and x_2 axes are parallel and orthogonal to the layering, respectively, so that the mth layer lies in the range $-d_m/2 \le x_2 \le d_m/2$. The generalized vector $\hat{\mathbf{y}}$ at the upper ($^+$) and lower ($^-$) boundaries of the layer is thus defined as

$$\hat{\mathbf{y}}^+_m = \hat{\mathbf{y}}(x_1, x_2 = \frac{d_m}{2}, \omega) = e^{\imath(k_1 x_1 + k_2\frac{d_m}{2})}\begin{bmatrix}\mathbf{0} & \mathbf{I}\\ \mathbf{C}_2 & \imath\mathbf{C}_2 k_2\end{bmatrix}e^{-\mathbf{D}_1^{-1}\mathbf{D}_0\frac{d_m}{2}}\mathbf{c}, \tag{17}$$

and

$$\hat{\mathbf{y}}^-_m = \hat{\mathbf{y}}(x_1, x_2 = -\frac{d_m}{2}, \omega) = e^{\imath(k_1 x_1 - k_2\frac{d_m}{2})}\begin{bmatrix}\mathbf{0} & \mathbf{I}\\ \mathbf{C}_2 & \imath\mathbf{C}_2 k_2\end{bmatrix}e^{\mathbf{D}_1^{-1}\mathbf{D}_0\frac{d_m}{2}}\mathbf{c}. \tag{18}$$

The vector of constants $\mathbf{c}$ is obtained from (18) as

$$\mathbf{c} = e^{-\mathbf{D}_1^{-1}\mathbf{D}_0\frac{d_m}{2}}\begin{bmatrix}\mathbf{0} & \mathbf{I}\\ \mathbf{C}_2 & \imath\mathbf{C}_2 k_2\end{bmatrix}^{-1}e^{-\imath(k_1 x_1 - k_2\frac{d_m}{2})}\hat{\mathbf{y}}^-_m, \tag{19}$$

and is then plugged in (17) resulting in

$$\hat{\mathbf{y}}^+_m = e^{\imath k_2 d_m}\begin{bmatrix}\mathbf{0} & \mathbf{I}\\ \mathbf{C}_2 & \imath\mathbf{C}_2 k_2\end{bmatrix}e^{-\mathbf{D}_1^{-1}\mathbf{D}_0 d_m}\begin{bmatrix}\mathbf{0} & \mathbf{I}\\ \mathbf{C}_2 & \imath\mathbf{C}_2 k_2\end{bmatrix}^{-1}\hat{\mathbf{y}}^-_m = \mathbf{T}^\Gamma_m\hat{\mathbf{y}}^-_m, \tag{20}$$

being $\mathbf{T}^\Gamma_m$ the transfer matrix of the single layer Γ depending both on the angular frequency ω and the wave number k_1. At this point, by recalling the continuity condition between adjacent layers, defined as

$$\hat{\mathbf{y}}^+_m = \hat{\mathbf{y}}^-_{m+1}, \tag{21}$$

it follows that the relation between the lower boundary of the first layer and the upper boundary of the nth layer results defined

$$\hat{\mathbf{y}}^+_n = \mathbf{T}_{(1,\mathcal{N}_n)}\hat{\mathbf{y}}^-_1, \tag{22}$$

with the (ω, k_1)-dependent transfer matrix of the entire elementary cell being defined as

$$\mathbf{T}_{(1,\mathcal{N}_n)} = \prod_{m=1}^{\mathcal{N}_n}\mathbf{T}^\Gamma_m, \tag{23}$$

where the index n unequivocally denotes the Fibonacci generation S_n made up of a number of elements equal to $\mathcal{N}_n = \frac{1}{\sqrt{5}}\left[\phi^{n-2} - \psi^{n-2} + \phi^{n-1} - \psi^{n-1}\right]$, with ϕ the golden mean, the auxiliary variable $\psi = -\frac{1}{\phi}$ and $n \ge 2$. Moreover, in order to consider the hierarchical waveguide characterized by an elementary cell consisting of the Fibonacci generation S_n, the Floquet–Bloch boundary conditions are exploited as

$$\hat{\mathbf{y}}^+_n = e^{\imath k_2 d}\hat{\mathbf{y}}^-_1, \tag{24}$$

being $d = \mathcal{N}^A_n d_A + \mathcal{N}^B_n d_B$ the characteristic size of the elementary cell in the direction perpendicular to the layering, where $\mathcal{N}^A_n = \frac{1}{\sqrt{5}}\left[\phi^{n-3} - \psi^{n-3} + \phi^{n-2} - \psi^{n-2}\right]$ and $\mathcal{N}^B_n = \mathcal{N}_n - \mathcal{N}^A_n$ are the numbers of building blocks A and B in the elementary cell, respectively.

By plugging (24) in (22), the following eigenproblem describing the propagation of Bloch waves is defined

$$\left(\mathbf{T}_{(1,\mathcal{N}_n)} - \mu\mathbf{I}\right)\hat{\mathbf{y}}^-_1 = \mathbf{0}, \tag{25}$$

where $\mathbf{I}$ is the identity matrix and $\mu = e^{\imath k_2 d}$ plays the role of the Floquet multiplier. In the particular case, of great applicative interest analyzed in the illustrative examples, of waves propagating along the direction orthogonal to the layering, i.e. with $k_1 = 0$, the problem (25) turns out to be standard linear eigenproblem, where μ is the eigenvalue and the wave form $\hat{\mathbf{y}}^-_1$ is the eigenvector. In such a context to ensure non-trivial solutions, the characteristic equation $\mathcal{P}(\mu) = \det(\mathbf{T}_{(1,\mathcal{N}_n)} - \mu\mathbf{I}) = 0$ must be satisfied. More specifically, the characteristic equation can be written in the form

$$\mathcal{P}(\mu) = I_0\mu^4 + I_1\mu^3 + I_2\mu^2 + I_3\mu + I_4, \tag{26}$$

where I_0, I_1, I_2, I_3 and I_4 are the principal invariants depending on the angular frequency ω. By recalling that the transfer matrix $\mathbf{T}_{(1,\mathcal{N}_n)}$ is symplectic, it follows that its characteristic polynomial is palindromic, so that the principal invariants fulfill the relations $I_0 = I_4 = 1$, $I_3 = I_1$. As known, if μ is a root of the characteristic polynomial, μ^{-1} is also a

root. Therefore, by exploiting the mapping $z = \mu + \mu^{-1}$, the following characteristic polynomial of reduced order is obtained

$$\widetilde{\mathcal{P}}(z) = z^2 + I_1 z + (I_2 - 2) = 0, \tag{27}$$

where the invariants I_1 and I_2 take the form

$$\begin{aligned} I_1 &= -\mathrm{tr}\left(\mathbf{T}_{(1,\mathcal{N}_n)}\right), \\ I_2 &= -\frac{1}{2}\mathrm{tr}\left(\mathbf{T}^2_{(1,\mathcal{N}_n)}\right) + \frac{1}{2}\left(\mathrm{tr}\left(\mathbf{T}_{(1,\mathcal{N}_n)}\right)\right)^2. \end{aligned} \tag{28}$$

After finding the roots of the reduced polynomial (27), recalling the inverse mapping $\mu = (z \pm \sqrt{z^2-4})/2$, the roots of polynomial (26) are unequivocally determined, as

$$\begin{aligned} \mu_{1,2} &= \frac{-I_1 + \sqrt{I_1^2 - 4(I_2-2)}}{4} \pm \frac{1}{4}\sqrt{\left(-I_1 + \sqrt{I_1^2 - 4(I_2-2)}\right)^2 - 16}, \\ \mu_{3,4} &= \frac{-I_1 - \sqrt{I_1^2 - 4(I_2-2)}}{4} \pm \frac{1}{4}\sqrt{\left(-I_1 - \sqrt{I_1^2 - 4(I_2-2)}\right)^2 - 16}. \end{aligned} \tag{29}$$

By exploiting the relation $\mu_\alpha = e^{\imath d k_2^{(\alpha)}}$, with $\alpha = 1, \dots, 4$, it is possible to determine the wave number $k_2^{(\alpha)}$, in terms of the angular frequency ω, as

$$k_2^{(\alpha)}(\omega) = \frac{\ln(\mu_\alpha(\omega))}{\imath d} = \frac{1}{d}\left(\arg(\mu_\alpha(\omega)) - \imath\frac{1}{2}\ln(|\mu_\alpha(\omega)|^2)\right), \tag{30}$$

defining the complex frequency band structure of the hierarchical waveguide within its periodicity range for $\Re(k_2) \in (-\pi/d, \pi/d]$, $\Im(k_2) \in \mathbb{R}$, and $\omega \in \mathbb{R}$. In the case of horizontal layers, with $\theta = 0$, it is possible to demonstrate that Eq. (22), after proper manipulations, specializes in

$$\begin{bmatrix} \hat{\mathbf{y}}^+_{nS} \\ \hat{\mathbf{y}}^+_{nC} \end{bmatrix} = \begin{bmatrix} \mathbf{T}^S_{(1,\mathcal{N}_n)} & \mathbf{0} \\ \mathbf{0} & \mathbf{T}^C_{(1,\mathcal{N}_n)} \end{bmatrix} \begin{bmatrix} \hat{\mathbf{y}}^-_{1S} \\ \hat{\mathbf{y}}^-_{1C} \end{bmatrix}, \tag{31}$$

being the vectors $\hat{\mathbf{y}}^\pm_{jS} = \left[\imath\hat{w}^\pm_{1(j)} \hat{\sigma}^\pm_{12(j)}\right]^T$, $\hat{\mathbf{y}}^+_{jC} = \left[\imath\hat{w}^\pm_{2(j)} \hat{\sigma}^\pm_{22(j)}\right]^T$ with j equal to 1 or n, and $\mathbf{T}^S_{(1,\mathcal{N}_n)}$, $\mathbf{T}^C_{(1,\mathcal{N}_n)}$ the 2×2 transfer matrices related to shear (S) and compressional (C) waves propagating along the $\mathbf{e}_2$ direction, respectively. It follows that two uncoupled eigenproblems are defined in the form

$$\left(\mathbf{T}^\Psi_{(1,\mathcal{N}_n)} - \mu\mathbf{I}\right)\hat{\mathbf{y}}^-_{1\Psi} = \mathbf{0}, \tag{32}$$

where Ψ is equal to S and C alternately. The corresponding characteristic polynomial is

$$\mathcal{P}^\Psi(\mu) = I_0^\Psi \mu^2 + I_1^\Psi \mu + I_2^\Psi, \tag{33}$$

where $I_0^\Psi = I_2^\Psi = 1$, and the invariant I_1^Ψ can be expressed as

$$I_1^\Psi = -\mathrm{tr}\left(\mathbf{T}^\Psi_{(1,\mathcal{N}_n)}\right). \tag{34}$$

Furthermore, it is worth pointing out that in order to determine the dispersion relation of Bloch waves characterized by a generic wave vector $\mathbf{k}$, it is possible to impose that the coefficients matrix of the homogeneous algebraic Eq. (25) is singular. In this way the so-called characteristic equation $\mathcal{F}(\mathbf{k},\omega) = \det\left(\mathbf{T}_{(1,\mathcal{N}_n)} - \lambda\mathbf{I}\right) = 0$ is obtained, where $\mathbf{k} \in \mathbb{C}^2$, and $\omega \in \mathbb{R}$, describing the dispersion relation in the implicit form. The complex spectrum is in general determined from the intersection of two hypersurfaces, fulfilling the following relation

$$\begin{cases} \mathrm{Re}\left(\mathcal{F}(\omega, \mathrm{Re}(k_1), \mathrm{Im}(k_1), \mathrm{Re}(k_2), \mathrm{Im}(k_2))\right) = 0 \\ \mathrm{Im}\left(\mathcal{F}(\omega, \mathrm{Re}(k_1), \mathrm{Im}(k_1), \mathrm{Re}(k_2), \mathrm{Im}(k_2))\right) = 0. \end{cases} \tag{35}$$

Note that, setting $k_2 = 0$ it is possible to determine the complex spectrum associated to waves propagating along the layering direction. This problem was also investigated, with an alternative procedure, for isotropic linear elastic layers in [73,75].

5. Illustrative examples

This Section is devoted to present some illustrative examples. Focus is on a class of Fibonacci-based hierarchical waveguides with building blocks A and B (with $d_A/d_B = 2$) made up as described below. Specifically, the building block B is made of a soft matrix of epoxy resin Epotek 301, a passive polymer material, with elastic properties E= 3.6 GPa and ν=0.35, dielectric constant β=3.187 $\cdot 10^{-11}$ C/(Vm) and mass density ρ=1150 kg/m^3, see [76]. On the other hand, the microstructured building block A is manufactured as follows. The layer A_1 is made of steel with E=210 GPa, ν=0.3, dielectric constant β=8.854 $\cdot 10^{-12}$ C/(Vm) and mass density ρ= 7500 kg/m^3.

Moreover, the layer A_2, i.e. the shunted piezoelectric element, is made of Polyvinylidene fluoride (PVDF) in parallel to an electrical circuit with purely capacitive equivalent admittance, as shown in Fig. 3(a). The electromechanical properties of PVDF, polarized along the out of plane direction, are taken from [77] and are listed below. The non vanishing components of the elasticity tensor are $C^{A_2}_{1111} = C^{A_2}_{2222}$ = 4.84 $\cdot 10^{09}$ Pa, $C^{A_2}_{3333}$ = 4.63$\cdot 10^9$ Pa, $C^{A_2}_{1122}$ = 2.72$\cdot 10^9$ Pa, $C^{A_2}_{1133} = C^{A_2}_{2233}$ = 2.22$\cdot 10^9$ Pa, $C^{A_2}_{1212}$=1.06$\cdot 10^9$ Pa, $C^{A_2}_{1313} = C^{A_2}_{2323}$ = 5.26$\cdot 10^7$ Pa. The non vanishing components of the stress-charge coupling tensor are $e^{A_2}_{113} = e^{A_2}_{223}$=-1.999 $\cdot 10^{-3}$ C/m^2, $e^{A_2}_{311} = e^{A_2}_{322}$=4.344 $\cdot 10^{-3}$ C/m^2, $e^{A_2}_{333}$=-1.099 $\cdot 10^{-1}$ C/m^2. Furthermore, the non vanishing components of the dielectric permittivity tensor are $\beta^{A_2}_{11} = \beta^{A_2}_{22}$= 6.641 $\cdot 10^{-11}$ C/Vm, and $\beta^{A_2}_{33}$=7.083 $\cdot 10^{-11}$ C/Vm.

More specifically, Section 5.1 is focused on the characterization of acoustic properties of the Fibonacci-based waveguide in the case of an equivalent electrical circuit with zero capacitance, i.e. with open circuit. Attention is paid to the influence of the orientation of the microstructured layers in the building block A on the frequency band structure of the periodically repeated Fibonacci generations $\mathcal{S}_j$, within the validity of scale separation principle and in the *high-fidelity frequency range*. Finally, in Section 5.2 the design of the high-performance acoustic waveguide is proposed. By modifying the tuning parameter, the constitutive properties of the piezoelectric shunting material can be adaptively controlled, as well as the dispersive properties of the hierarchical Fibonacci-like tunable superlattice.

5.1. Frequency band structure

We initially focus on the case in which the tuning parameter λ vanishes, corresponding to a non shunted piezoelectric material. In this framework, in Fig. 4 the frequency band structure in terms of the dimensionless frequency ω/ω_r (with $\omega_r = \left(2d_B\sqrt{\rho^B/E^B}\right)^{-1}$ and the apex referring to the building block B) is investigated, as the generation varies between $\mathcal{S}_2$ and $\mathcal{S}_7$, for the orientation angle $\theta = 0$. As already shown in Eq. (31), in this case the transfer matrix is block diagonal, and therefore it is possible to investigate the shear and compressional wave propagation in an uncoupled way. The frequency band structure associated to waves propagating in the direction perpendicular to the main stratification, that is characterized by a wave vector $\mathbf{k} = k_2\mathbf{e}_2$, are shown in Fig. 4(a) and Fig. 4(b), for shear and compressional waves respectively. It is important to note that, for both the set of spectra, frequency ranges that fall into band gaps for all generations after a certain generation $\mathcal{S}_\alpha$, with $\alpha \in \mathcal{N}^*$ are found. The band gaps containing these frequency ranges for the various subsequent generations with $\alpha > 2$ are referred to as *main band gaps* (pointed out with the repeated number 3). Moreover, in the particular case where $\alpha = 2$ they are referred to as *full main band gaps* (pointed out with numbers 1 and 2). The main band gaps and/or the full main band gaps delimit areas of the spectrum (highlighted by the colored boxes) within which each pass band (black rectangles), going from one generation to the next, fragments giving rise to an increasing number of pass band that follows the recursive rule of Fibonacci numbers ie 1, 1, 2, 3, 5, 8, ... For both these class of band gaps, it is in general observed that the

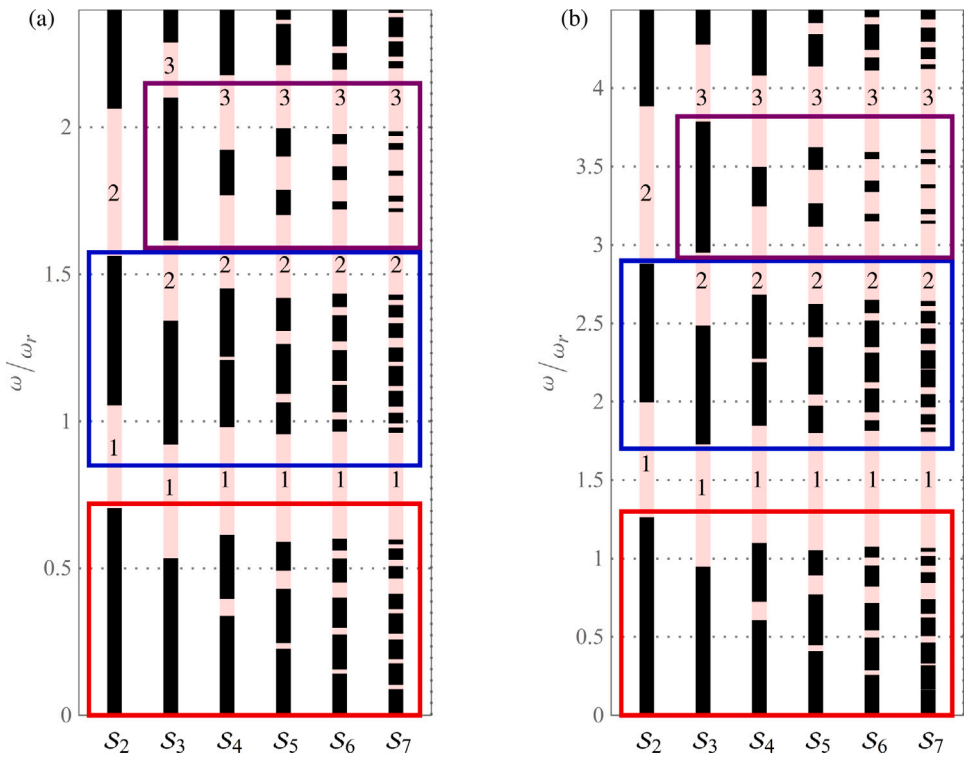

Fig. 4. Frequency band structure for waves characterized by a wave vector $\mathbf{k} = k_2\mathbf{e}_2$ with $\lambda = 0$, $\theta = 0$ and generations ranging from $\mathcal{S}_2$ to $\mathcal{S}_7$. (a) Shear waves; (b) Compressional waves.

amplitude remains approximately unchanged across generations, while the central frequency undergoes a clear reduction between the $\mathcal{S}_\alpha$ and the $\mathcal{S}_{\alpha+1}$ generations and then stabilizes on a certain value.

Furthermore, considering the second full main band gaps, between $\mathcal{S}_2$ and $\mathcal{S}_3$, a considerable amplitude reduction both for shear and compressional waves. As expected, the frequencies that define the limits of the pass bands associated with the compression waves are greater than the corresponding ones of the shear waves. By the way of example, referring to the case of shear waves already reported in Fig. 4(a), the frequency band structure associated to generations $\mathcal{S}_2 - \mathcal{S}_7$ is shown in Fig. 5. It is confirmed the fragmentation of the frequency spectrum, between two subsequent main band gaps, as the generation number increases, as well as it is noted that with the growth of generation numbers, the branches of the dispersion spectra become flatter. Moreover, the band gap zones are reported versus θ for different generations of the Fibonacci-like superlattice in Appendix.

The frequency spectrum accounting for both shear and compressional waves, characterized by a wave vector $\mathbf{k} = k_2\mathbf{e}_2$, is determined according to Eq. (30) and is shown in Fig. 6 as the angle θ changes. More specifically, Figs. 6(a), (b), (c), (d) refer to $\theta = 0, \pi/6, \pi/4, \pi/2$, respectively. As it clearly emerges from Eq. (5), when $\theta \in (0, \pi/2)$ the building block A is characterized by anisotropic constitutive tensors, while when $\theta = 0, \pi/2$ it is orthotropic with evident outcomes on spectral dispersive properties of the Fibonacci-based hierarchical waveguide. Also in this case it is possible to find full main band gaps, the first of which is numbered in figure. Its amplitude tends to remain constant, while the central frequency tends to decrease compared to the first generation. It can also be observed that in Fig. 6(b), corresponding to $\theta = \pi/6$, the full main band gap is split in two in $\mathcal{S}_6$ by a pass band associated with an almost local mode with approximately evanescent bandwidth. Differently from before, the areas of the spectrum between two main band gaps and/or full main band gaps no longer respect the Fibonacci recursive rule relative to the number of pass bands in successive generations. It is noteworthy that the same applies also in the case of $\theta = 0$ for which the diagram is shown in Fig. 6(a). Irrespective of θ, as the order of generation increases, on the one hand there is an increase in the overall amplitude associated with the various stop bands that fall within the frequency range considered and, on the other hand, as expected, an increasing complexity and jaggedness of the frequency spectrum.

5.2. Wave propagation control

Attention is now focused on the comparison between the frequency band structure obtained for $\lambda = 0$, i.e. in the case of non shunted piezoelectric phase $A1$, and $\lambda \to \lambda_R^+$ (with $\lambda_R \simeq -1.0368$ for shunted phase made of PVDF polarized along the out of plane direction) for generations $\mathcal{S}_2$ and $\mathcal{S}_3$, as the angle θ changes.

First the case of generation $\mathcal{S}_2$ is considered. In Fig. 7(a) and 7(b) the band gap zones for $\lambda = 0$ and $\lambda \to \lambda_R^+$ are reported, respectively, versus θ. In general, it emerges that, as λ tends to λ_R^+, the low-frequency band gap zones become noticeably wider, thus demonstrating the effectiveness of the tunable metamaterial as acoustic waveguide as θ varies. In fact, very high amplifications are noted for a wide range of θ. As an example, note that for values of $\theta \simeq \pi/4$ the amplification factor is about 7, for $\theta \simeq 3\pi/8$ is about 10, while for $\theta \simeq 5\pi/6$ for $\lambda = 0$ the band gap is practically evanescent, whereas for $\lambda \to \lambda_R^+$ it becomes comparable with the maximum value. On the other hand, for θ values about 0 and $\pi/2$ it emerges, as expected, a reduced effect of the tunable electrical circuit. For $\theta \approx 0$ and $\theta \approx \pi/2$, indeed, the building block A is characterized by orthotropic constitutive tensors, thus the tuning parameter λ does not influence the dispersion curves associated with shear waves, as it emerges from Eqs. (3)–(5). Moreover, it is observed that moving from $\lambda = 0$ to $\lambda \to \lambda_R^+$, the maximum value of the first band gap amplitude is shifted from $\theta \simeq \pi/10$ to $\theta \simeq \pi/4$. Interestingly, a symmetrization of the band gap zones with respect to $\theta \approx \pi/4$ in frequency range considered is observed.

Additionally, for $\lambda = 0$ in Fig. 8(a) and $\lambda \to \lambda_R^+$ in Fig. 8(b) plots of Floquet–Bloch spectrum in terms of the dimensionless frequency ω/ω_r versus the dimensionless wave number $k_2 d$ are reported for to

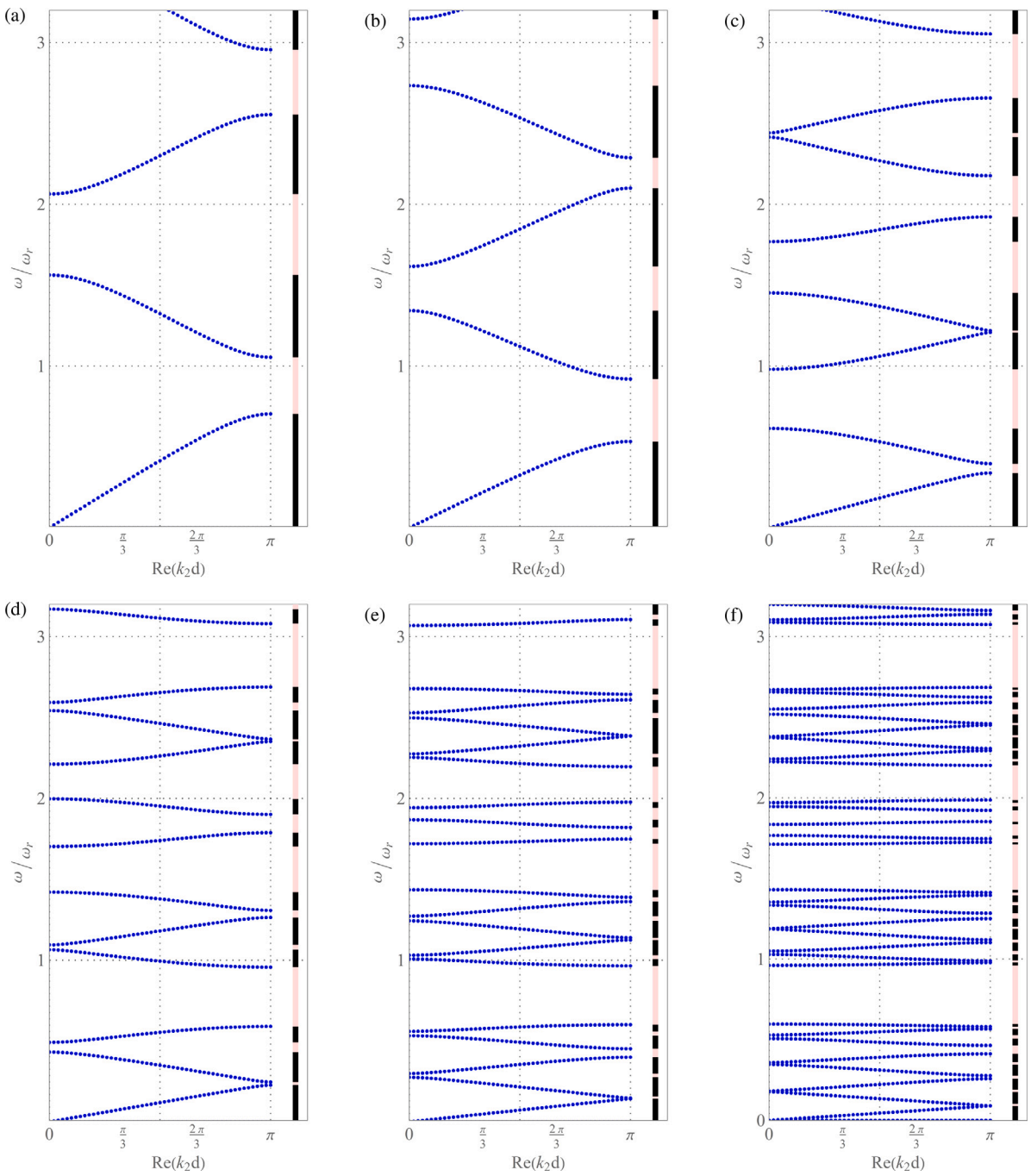

Fig. 5. Floquet–Bloch spectra for shear waves characterized by a wave vector $\mathbf{k} = k_2\mathbf{e}_2$ with $\lambda = 0$, $\theta = 0$ for different generations: (a) $\mathcal{S}_2$; (b) $\mathcal{S}_3$; (c) $\mathcal{S}_4$; (d) $\mathcal{S}_5$; (e) $\mathcal{S}_6$; (f) $\mathcal{S}_7$.

$\theta = 0, \pi/6, \pi/4, \pi/2$ in red, green, blue and black, respectively for a wide range of frequencies. More specifically, it emerges that for $\theta = 0, \pi/2$, the first band gap falls within the 1st and the 2nd optical branches, while for $\theta \in (0, \pi/2)$ it falls within the 2nd acoustic and the 1st optical branches. Focusing on the case with $\theta = \pi/4$, in Fig. 9 the frequency band structure for $\lambda = 0$ and $\lambda \to \lambda_R^+$ are compared. In this case for $\lambda = 0$, Fig. 9(a), ten stop bands are detected in the frequency range considered. On the other hand, it emerges that moving to $\lambda \to \lambda_R^+$, Fig. 9(b), a considerable lower spectral density is shown for the optical branches, and in general the band gap amplitudes tend to amplify, as also noted for the low frequency band gap, between the 2nd acoustic and the 1st optical branches. Besides, the first pass band amplitude remains almost the same as a function of λ, while in the considered frequency range pass band amplitude related to optical branches tend to decrease.

As a further investigation, we focus on both dimensionless band gap amplitude A_s/ω_r and central frequency $\overline{\omega}/\omega_r$ with respect to the tuning parameter $\lambda^* = \lambda - \lambda_R$. In Fig. 10 the blue curves refer to first band gap while the red curves to second one. Concerning the first band gap, it can be noted that both the band gap amplitude, Fig. 10(a), and the central frequency, Fig. 10(b), increase as λ^* decreases, i.e. when λ tends to λ_R. Focusing on the second gap, on the one hand it is confirmed that when λ approaches to λ_R the dimensionless band gap amplitude takes a maximum value, but, on the other hand, a qualitative different behavior is exhibited. It is, indeed, noted that for $\lambda^* \approx 0.0017$ the amplitude A_s/ω_r tends to vanish. The trend of $\overline{\omega}/\omega_r$ remains qualitatively similar

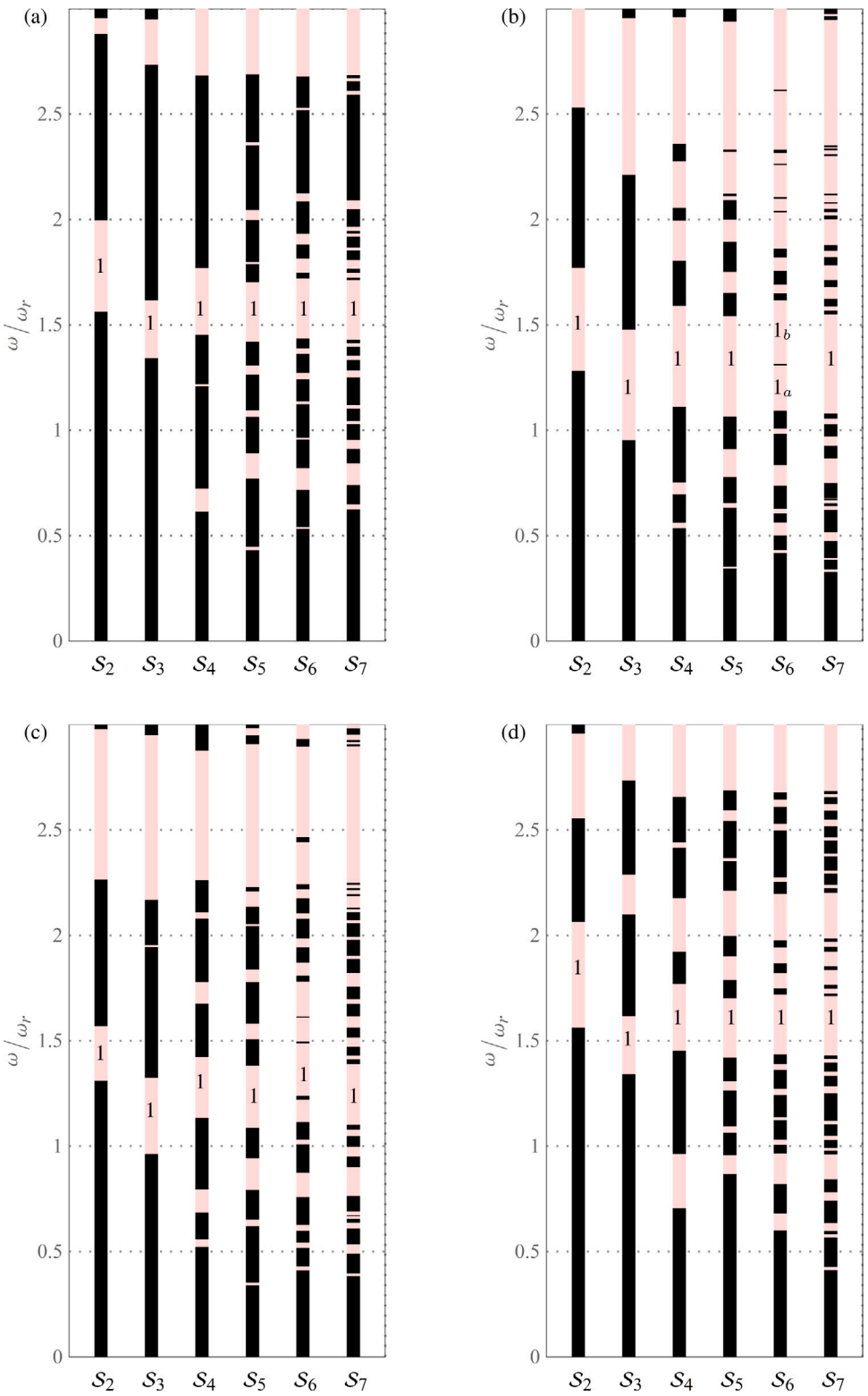

Fig. 6. Frequency band structure for waves characterized by a wave vector $\mathbf{k} = k_2\mathbf{e}_2$ with $\lambda = 0$ and generations ranging from S_2 to S_7. (a) θ=0; (b) $\theta = \pi/6$; (c) $\theta = \pi/4$; (d) $\theta = \pi$.

to the corresponding one exhibited by the first band gap except for $\lambda^* \approx 0.0017$, highlighted with a gray dot.

Now focus is on investigating the behavior of the generation S_3. Again in Fig. 11 the comparison between the frequency band structure corresponding to $\lambda = 0$ and $\lambda \to \lambda_R^+$ is performed as θ varies. As λ tends to approach λ_R, the low-frequency band gap zones extends over a wider range of θ. Also in this case the tunable metamaterial delivers very satisfactory performances, see Figs. 11(a) and (b). Again high amplifications of band gap amplitudes are noted for a wide range of θ. More specifically, for $\theta \simeq \pi/10$, corresponding to the maximum amplitude for $\lambda = 0$, the amplification factor is about 1.2, for $\theta \simeq \pi/4$ the amplification factor achieves the value of about 2.3, while for $\theta \simeq 2\pi/5$

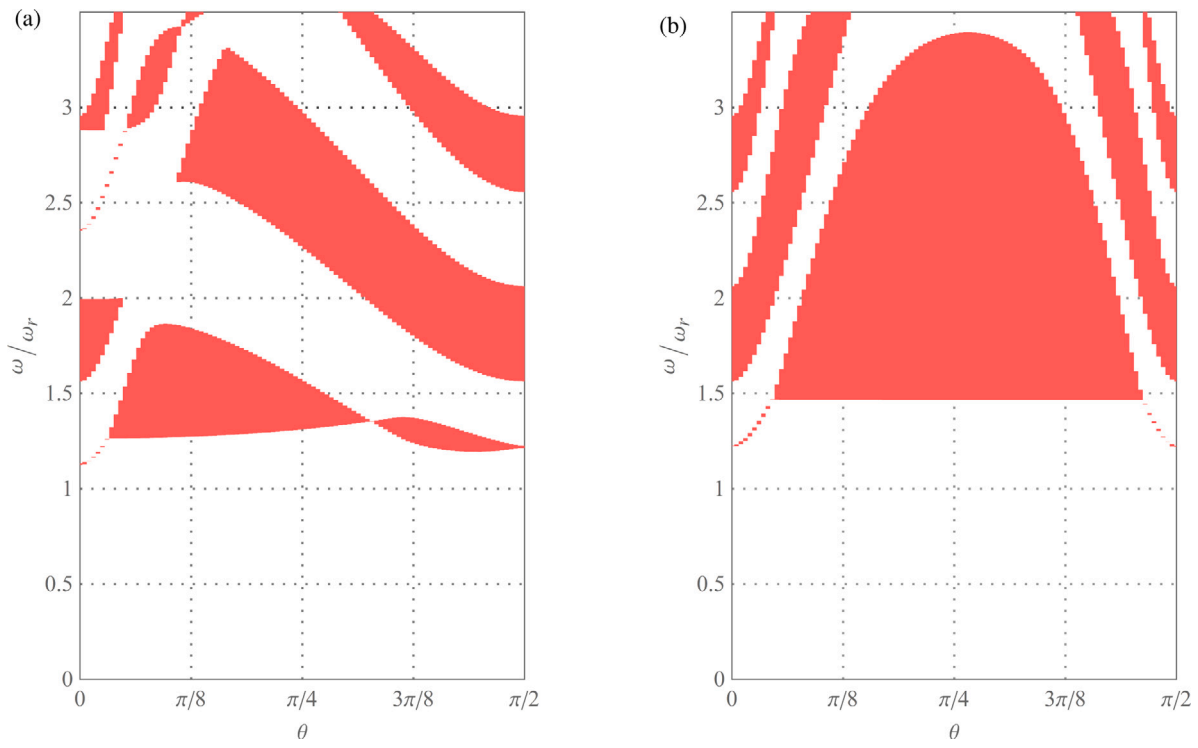

Fig. 7. Comparison between $\lambda = 0$ and $\lambda \to \lambda_R^+$ for the case of generation S_2. Band gap zones as θ varies. (a) $\lambda = 0$; (b) $\lambda \to \lambda_R^+$.

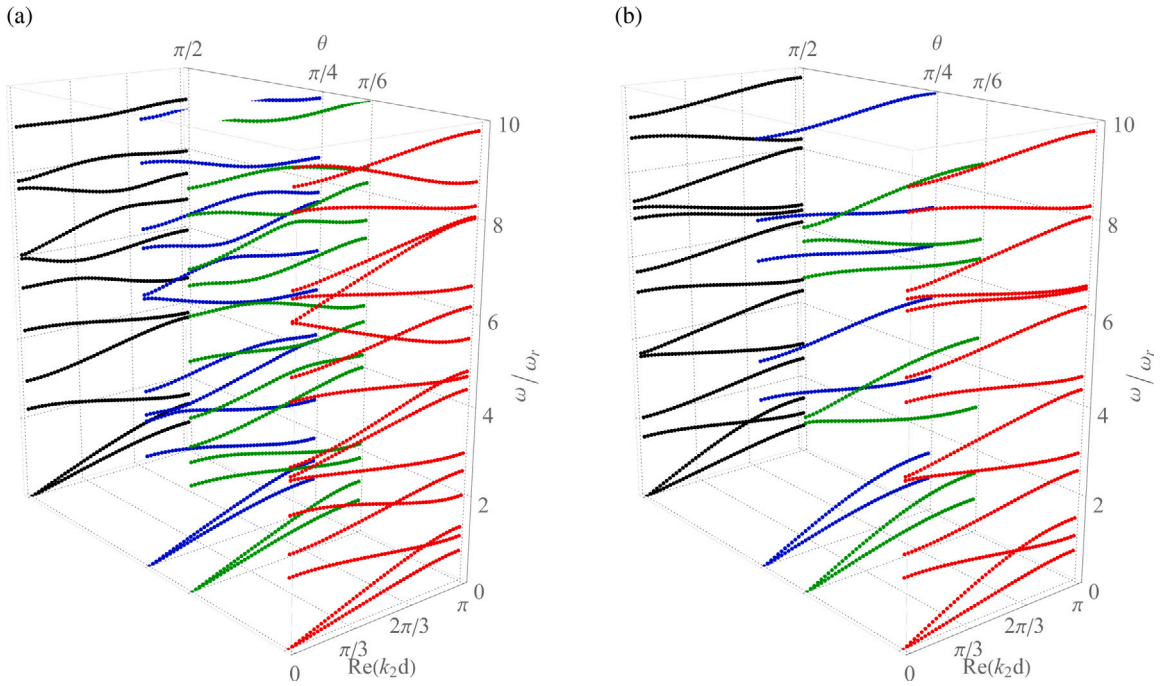

Fig. 8. Comparison between $\lambda = 0$ and $\lambda \to \lambda_R^+$ for the case of generation S_2. Floquet–Bloch spectra for $\theta = 0, \pi/6, \pi/4, \pi/2$. (a) $\lambda = 0$; (b) $\lambda \to \lambda_R^+$.

when $\lambda = 0$ the band gap is practically evanescent, whereas for $\lambda \to \lambda_R^+$ it becomes comparable with the maximum value. Also in this case, it can be observed that for θ values about 0 and $\pi/2$, corresponding to the case where the building block A has orthotropic constitutive tensors, the tunable electrical circuit exhibits a lower effectiveness, due to the lack of influence of the tuning parameter λ on the dispersion curves associated with shear waves, see Eqs. (3)–(5).

Additionally, for $\lambda = 0$ in Fig. 12(a) and $\lambda \to \lambda_R^+$ in Fig. 12(b) plots of Floquet–Bloch spectrum in terms of the dimensionless frequency ω/ω_r versus the dimensionless wave number $k_2 d$ are plot for to $\theta = 0, \pi/6, \pi/4, \pi/2$ in red, green, blue and black, respectively for a wide range of frequencies. Also in this case, it is observed that for $\theta = 0, \pi/2$ the first band gap falls within the 1st and the 2nd optical branches, while for $\theta \in (0, \pi/2)$ it falls within the 2nd acoustic and the 1st optical branches.

Considering the case with $\theta = \pi/4$, in Fig. 13(a) and (b) the frequency band structure for λ=0 and $\lambda \to \lambda_R^+$ are compared. In Fig. 13(a) with $\lambda = 0$, ten band gaps are found in the frequency range

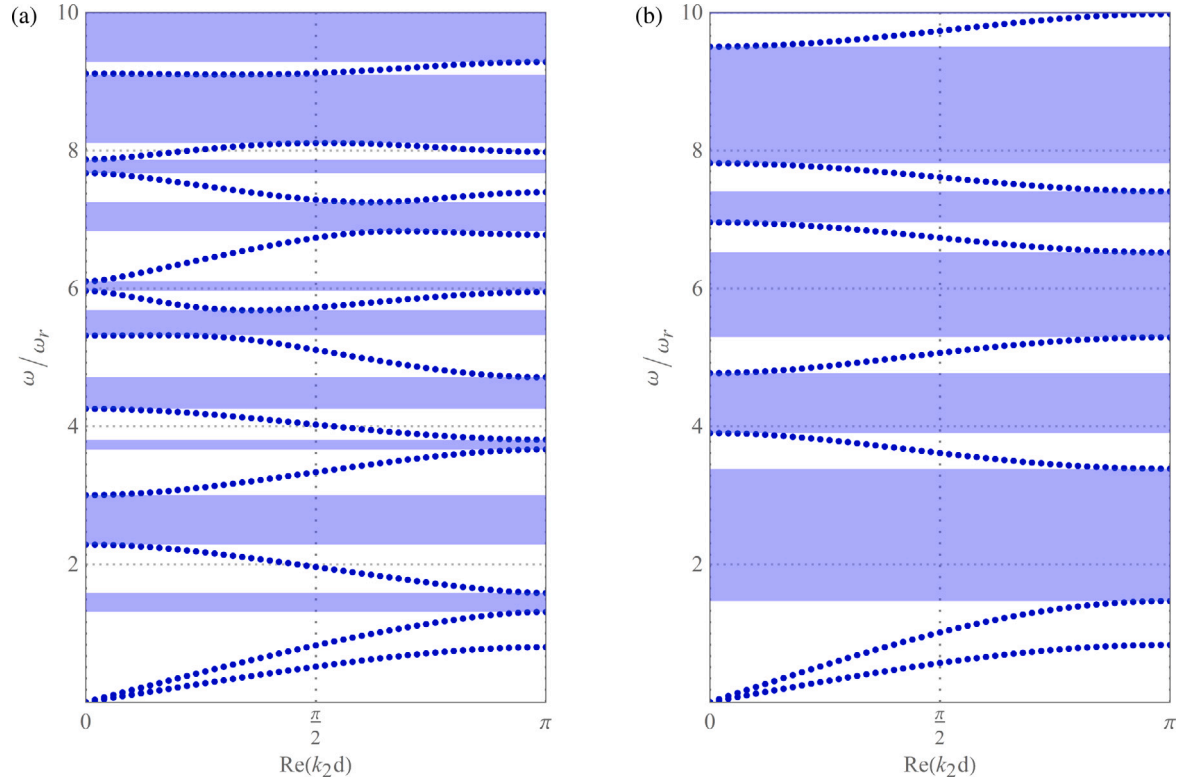

Fig. 9. Floquet–Bloch spectra, with stop bands highlighted in blue, for generation S_2 and $\theta = \pi/4$: (a) $\lambda = 0$; (b) $\lambda \to \lambda_R^+$.

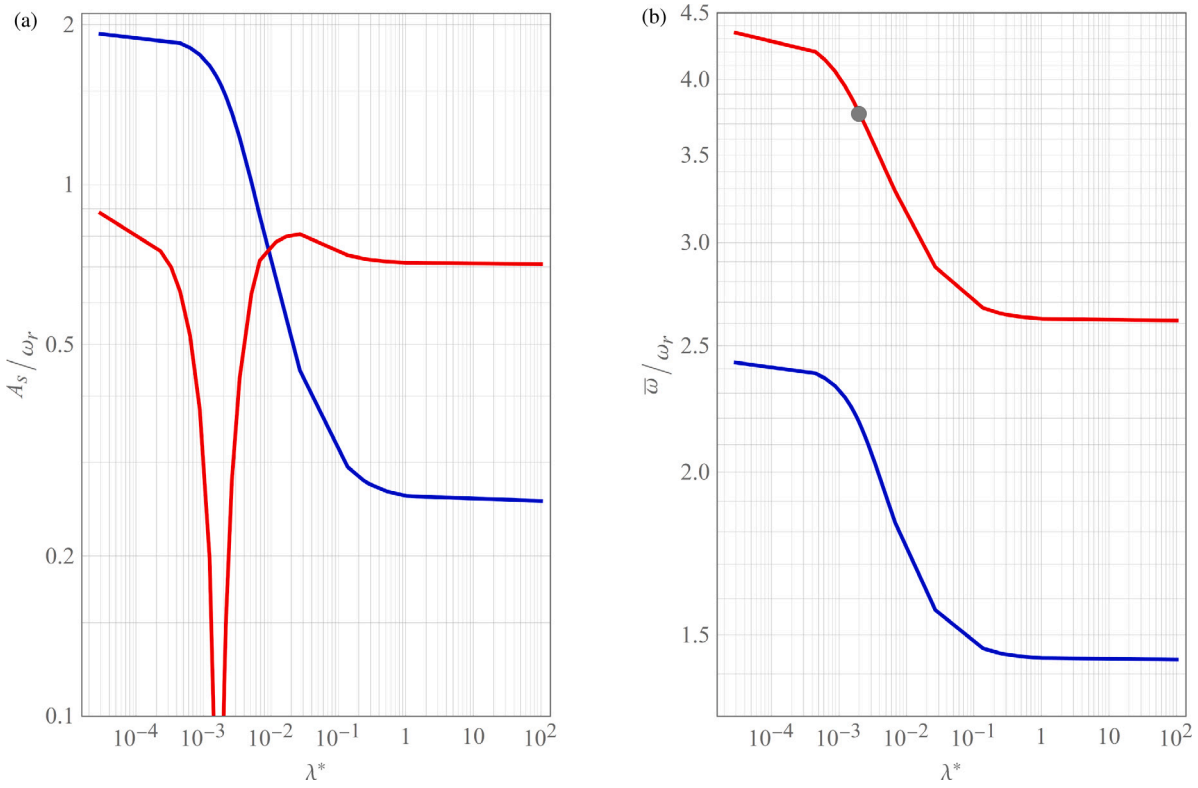

Fig. 10. First (red curves) and second (blue curves) band gaps, for waves characterized by a wave vector $\mathbf{k} = k_2 \mathbf{e}_2$, for generation S_2 and $\theta = \pi/4$: (a) dimensionless band gap amplitude A_s/ω_r as a function of λ^*; (b) central frequency $\overline{\omega}/\omega_r$ as a function of λ^*.

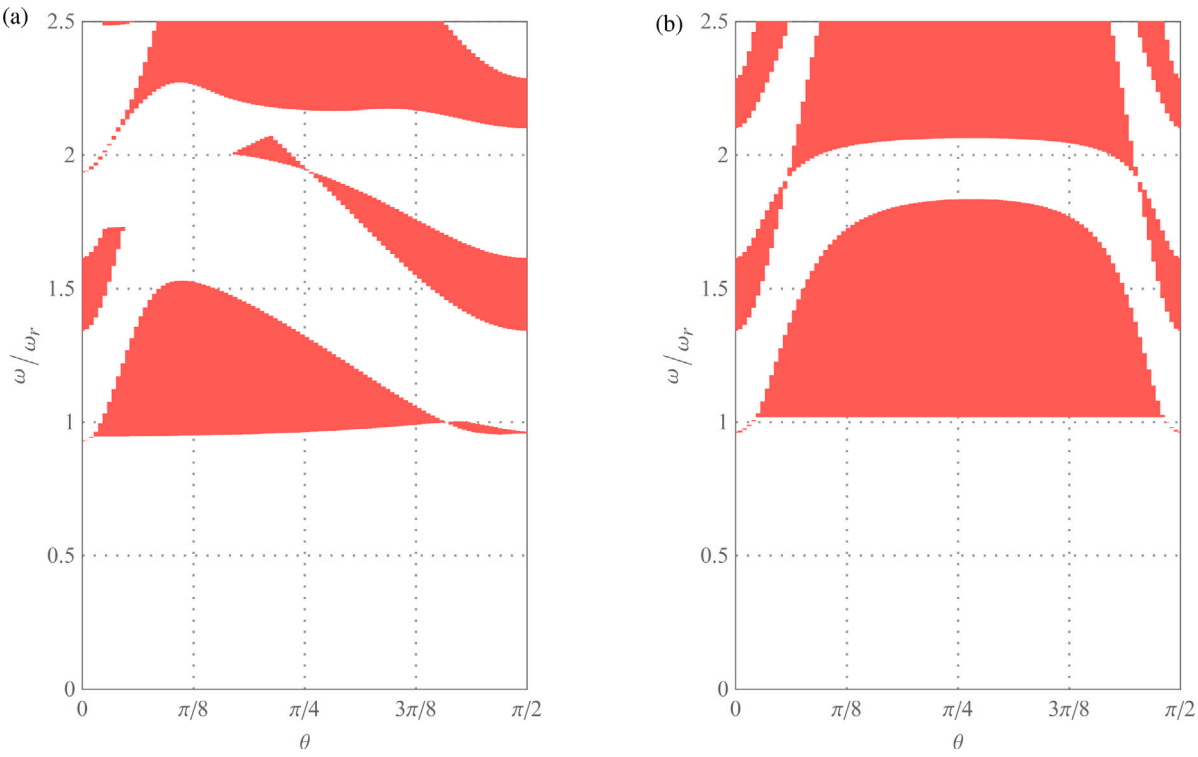

Fig. 11. Comparison between $\lambda = 0$ and $\lambda \to \lambda_R^+$ for the case of generation S_3. Band gap zones as θ varies. (a) $\lambda = 0$; (b) $\lambda \to \lambda_R^+$.

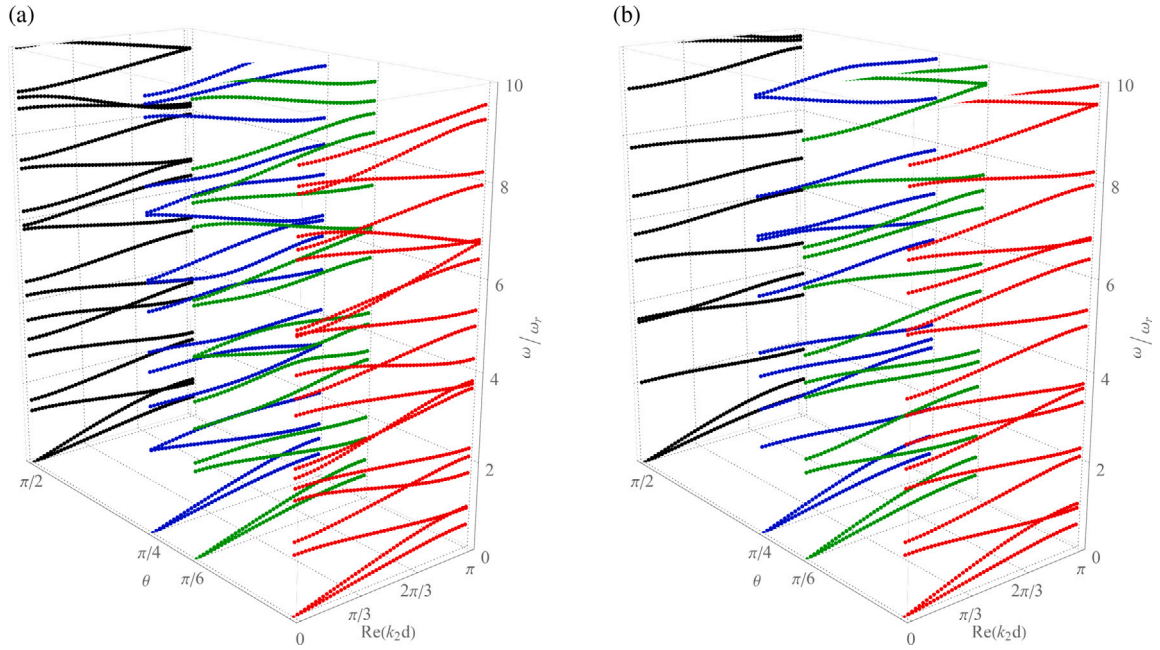

Fig. 12. Comparison between $\lambda = 0$ and $\lambda \to \lambda_R^+$ for the case of generation S_3. Floquet–Bloch spectra for $\theta = 0, \pi/6, \pi/4, \pi/2$. (a) $\lambda = 0$; (b) $\lambda \approx \lambda_R$.

considered. It stands to reason that for $\lambda \to \lambda_R^+$, see Fig. 13(b), a considerable lower spectral density is observed for the optical branches, as well as the band gap amplitudes tends to amplify, as clearly detected in the case of low-frequency band gap, between the 2nd acoustic and the first 1st optical branches.

In Fig. 14 both dimensionless band gap amplitude A_s/ω_r and central frequency $\overline{\omega}/\omega_r$ versus the tuning parameter $\lambda^* = \lambda - \lambda_R$ are shown. Again blue curves refer to the first band gap, while red curves refers to the second one. For both band gaps the band gap amplitude, Fig. 14(a), and the central frequency, Fig. 14(b), increase as λ^* decreases.

6. Final remarks

New hierarchical waveguides are designed to be used as high performances acoustic filters for the adaptive passive control of wave propagation. At the macroscopic scale the composite material is made of the periodic repetition, along a given periodicity direction, of two different building blocks arranged according to the Fibonacci recursive rule and forming a hierarchical layered material. Assuming the scale-separation, at the microscopic scale one building block is, in turn, a generically oriented layered two-phase composite with a piezoelectric

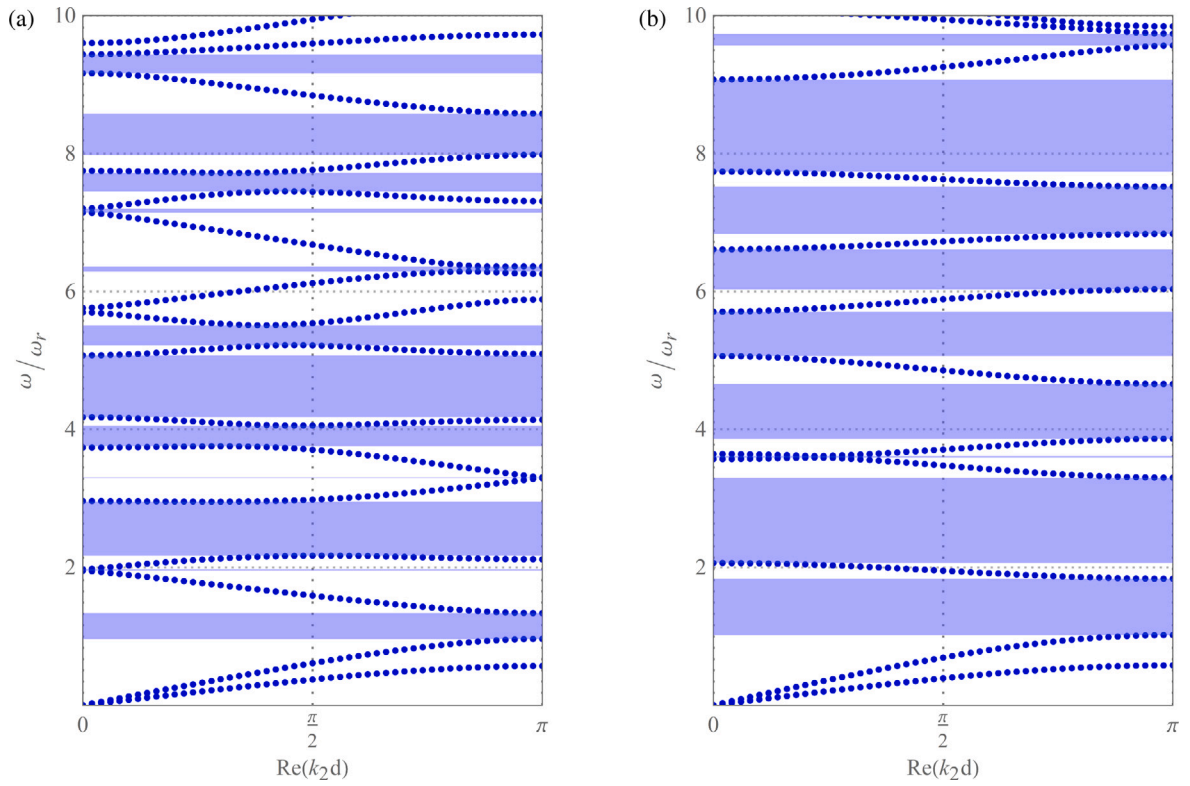

Fig. 13. Floquet–Bloch spectra, with stop bands highlighted in blue, for generation S_3 and $\theta = \pi/4$: (a) $\lambda = 0$; (b) $\lambda \to \lambda_R^+$.

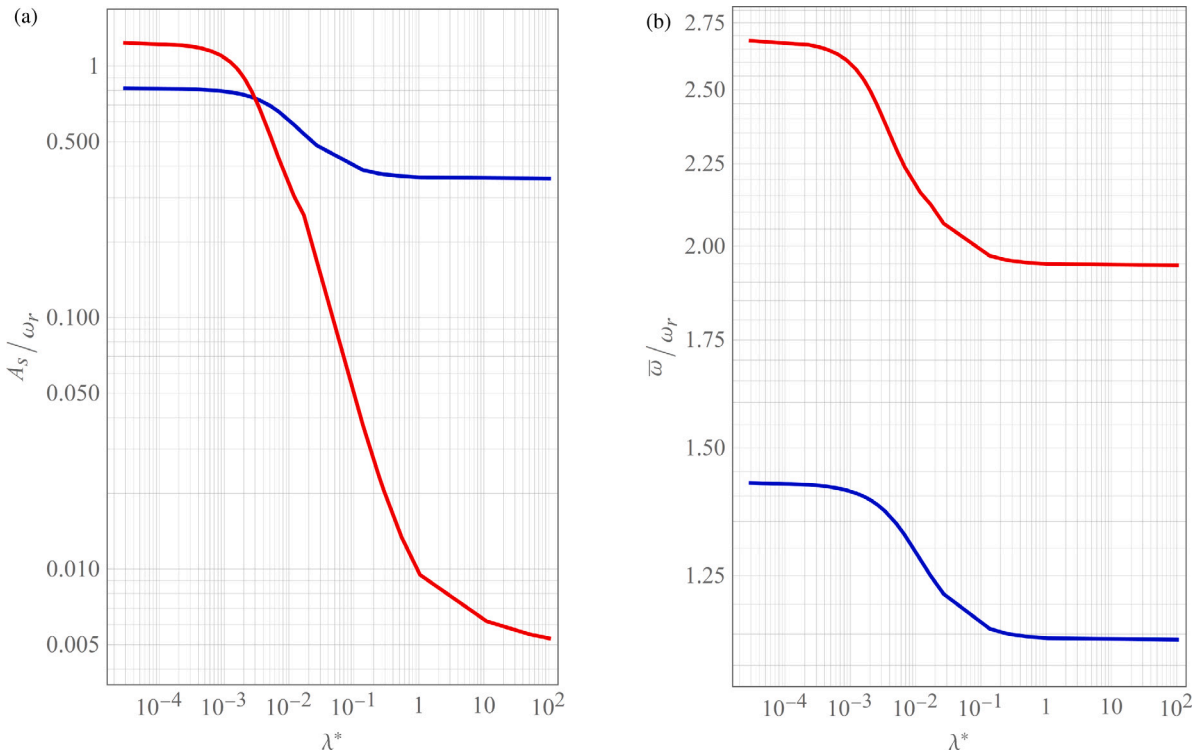

Fig. 14. First (red curves) and second (blue curves) band gaps, for waves characterized by a wave vector $\mathbf{k} = k_2 \mathbf{e}_2$, for generation S_3 and $\theta = \pi/4$: (a) dimensionless band gap amplitude A_s/ω_r as a function of λ^*; (b) central frequency $\bar{\omega}/\omega_r$ as a function of λ^*.

phase shunted by an electrical circuit. The first order homogenized physical properties of such layered microstructure are first determined exploiting an asymptotic homogenization scheme. Then, the acoustic dispersion properties of the waveguide are investigated by using a transfer matrix approach. In this framework, the frequency band structure is determined for different generations of the Fibonacci sequence and for different values of the angle measuring the orientation of the layered two-phase composite with respect to the macroscopic

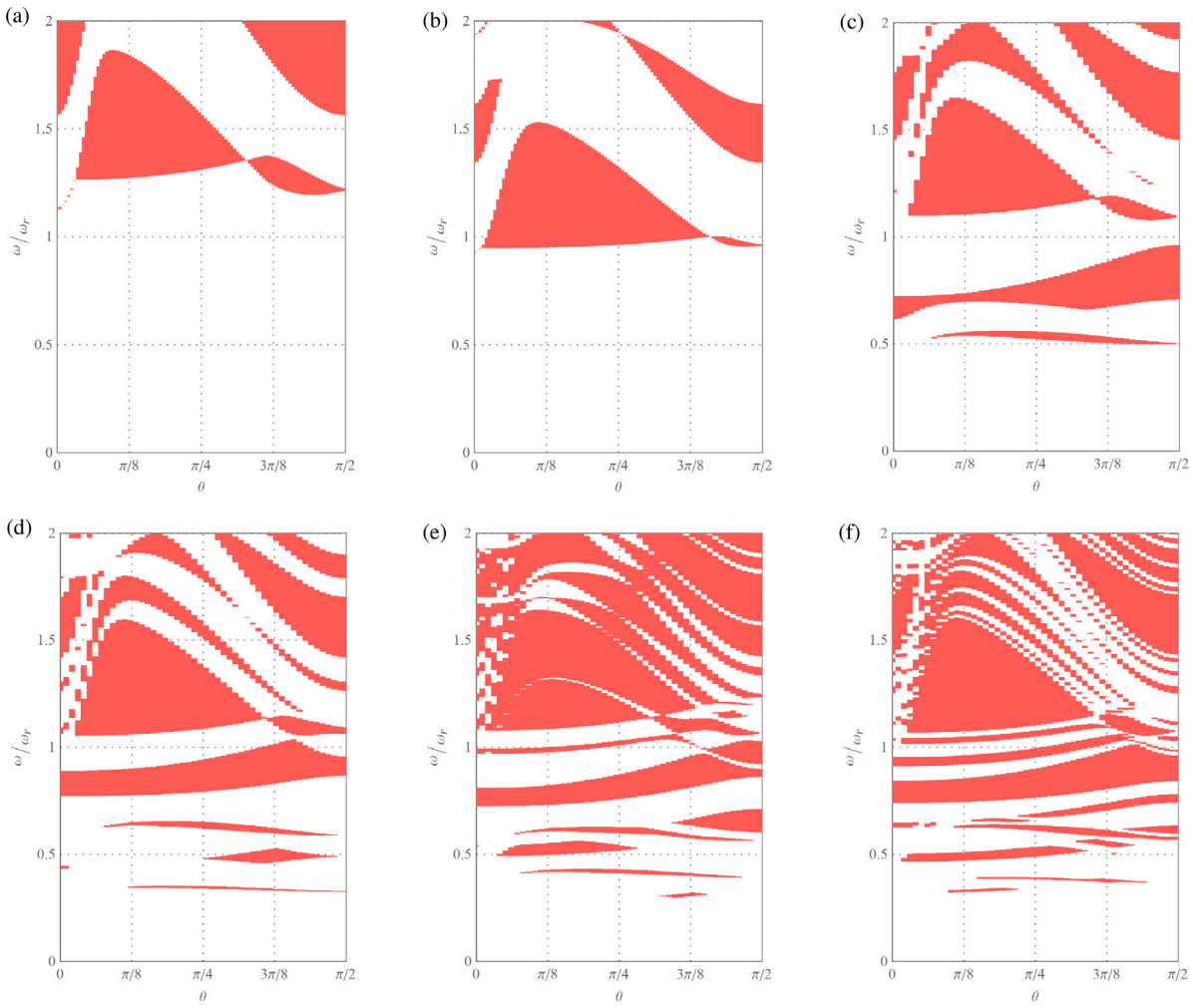

Fig. 15. Band gap zones as θ varies, with $\lambda = 0$, for different generations: (a) $\mathcal{S}_2$; (b) $\mathcal{S}_3$; (c) $\mathcal{S}_4$; (d) $\mathcal{S}_5$; (e) $\mathcal{S}_6$; (f) $\mathcal{S}_7$.

hierarchical layered material. It emerges that, when the layers at the two scales share the same orientation and shear and compressional waves are separately investigated, the main band gaps delimit areas of the frequency spectrum in which, passing from one generation to the next, each pass band splits into a number of shorter ones consistently with the recursive rule of Fibonacci numbers. On the other hand, as soon as the layers at the two scales have different orientation such properties, as expected, are lost. In both cases, with the growth of generation numbers, the number of pass and stop bands increases and, in general, the dispersion branches of the spectra become flatter. The effectiveness of the tunable metamaterial as acoustic waveguide is further tested, for different Fibonacci generations, in the relevant case of purely capacitive non dissipative electrical circuit. It is proved that as the tuning parameter approaches the resonance value, the hierarchical waveguide exhibits strongly improved performances, with the best behavior delivered for the case the orientation of layers at the two scales differs by $\pi/4$. The promising results obtained from the characterization of the proposed new hierarchical Fibonacci-based layered material are crucial for the optimal design of tunable acoustic filters, adapt to a variable performance requirement in real-time.

Declaration of competing interest

The authors declare that they have no known competing financial interests or personal relationships that could have appeared to influence the work reported in this paper.

Acknowledgments

The authors gratefully acknowledge financial support from project Search for Excellence Ud'A 2019 University of Chieti-Pescara, National Group of Mathematical Physics, Italy (GNFM-INdAM), from the Compagnia San Paolo, Italy, project MINIERA no. I34I20000380007, from University of Trento, project UNMASKED 2020.

Appendix. Band gap zones for different generations and $\lambda = 0$

In Fig. 15, the band gap zones for $\lambda = 0$ are reported versus $\theta$for different generations of the Fibonacci-like superlattice. In general, it emerges that, as the generation number increases the frequency band structure appears more and more fragmented, accordingly with the behavior showed by the frequency spectrum shown in Fig. 5 for $\theta = 0$.

References

[1] Magid LM. Mechanical energy flow in crystal lattices. Phys Rev 1964;134:A158–62.
[2] Langley RS. A transfer matrix analysis of the energetics of structural wave motion and harmonic vibration. Proc R Soc Lond Ser A Math Phys Eng Sci 1996;452(1950):1631–48.
[3] Ostoja-Starzewski M. Lattice models in micromechanics. Appl Mech Rev 2002;55(1):35–60.
[4] Martinsson P, Movchan AB. Vibrations of lattice structures and phononic band gaps. Q J Mech Appl Math 2003;56.1:45–64.

[5] Ruzzene M, Scarpa F, Soranna F. Wave beaming effects in two-dimensional cellular structures. Smart Mater Struct 2003;12(3):363–72.
[6] Tee KF, Spadoni A, Scarpa F, Ruzzene M. Wave propagation in auxetic tetrachiral honeycombs. J Vib Acoust 2010;132(3). 031007.
[7] Demmie PN, Ostoja-Starzewski M. Waves in fractal media. J Elasticity 2011;104(1–2):187–204.
[8] Allegri G, Scarpa F, Chowdhury R, Adhikari S. Wave propagation in periodically supported nanoribbons: A nonlocal elasticity approach. J Vib Acoust 2013;135(4):041017.
[9] Lemoult F, Kaina N, Fink M, Lerosey G. Wave propagation control at the deep subwavelength scale in metamaterials. Nat Phys 2013;9(1):55.
[10] De Bellis ML, Bacigalupo A. Auxetic behavior and acoustic properties of microstructured piezoelectric strain sensors. Smart Mater Struct 2017;26(8):085037.
[11] Bacigalupo A, Gambarotta L. Dispersive wave propagation in two-dimensional rigid periodic blocky materials with elastic interfaces. J Mech Phys Solids 2017;102:165–86.
[12] Bacigalupo A, Gambarotta L. Wave propagation in non-centrosymmetric beam-lattices with lumped masses: discrete and micropolar modeling. Int J Solids Struct 2017;118:128–45.
[13] Tol S, Degertekin F, Erturk A. Phononic crystal luneburg lens for omnidirectional elastic wave focusing and energy harvesting. Appl Phys Lett 2017;111(1):013503.
[14] Bacigalupo A, Lepidi M. Acoustic wave polarization and energy flow in periodic beam lattice materials. Int J Solids Struct 2018;147:183–203.
[15] D'Alessandro L, Zega V, Ardito R, Corigliano A. 3D auxetic single material periodic structure with ultra-wide tunable bandgap. Sci Rep 2018;8(1):2262.
[16] Bacigalupo A, De Bellis ML, Gnecco G. Complex frequency band structure of periodic thermo-diffusive materials by Floquet–Bloch theory. Acta Mech 2019;230(9):3339–63.
[17] Bordiga G, Cabras L, Bigoni D, Piccolroaz A. Free and forced wave propagation in a Rayleigh-beam grid: Flat bands, Dirac cones, and vibration localization vs isotropization. Int J Solids Struct 2019;161:64–81.
[18] Dal Corso F, Tallarico D, Movchan NV, Movchan AB, Bigoni D. Nested Bloch waves in elastic structures with configurational forces. Phil Trans R Soc A 2019;377(2156):20190101.
[19] Kamotski IV, Smyshlyaev VP. Bandgaps in two-dimensional high-contrast periodic elastic beam lattice materials. J Mech Phys Solids 2019;123:292–304, The N.A. Fleck 60th Anniversary Volume.
[20] Park HW, Oh JH. Study of abnormal group velocities in flexural metamaterials. Sci Rep 2019;9:13973.
[21] Liu XN, Hu GK, Sun CT, Huang GL. Wave propagation characterization and design of two-dimensional elastic chiral metacomposite. J Sound Vib 2011;330(11):2536–53.
[22] Norris AN, Shuvalov AL. Elastic cloaking theory. Wave Motion 2011;48:525–38.
[23] Christensen J, García de Abajo FJ. Negative refraction and backward waves in layered acoustic metamaterials. Phys Rev B 2012;86:024301.
[24] Stenger N, Wilhelm M, Wegener M. Experiments on elastic cloaking in thin plates. Phys Rev Lett 2012;108(1):014301.
[25] Yan X, Zhu R, Huang G, Yuan FG. Focusing guided waves using surface bonded elastic metamaterials. Appl Phys Lett 2013;103(12):121901.
[26] Colquitt D, Brun M, Gei M, Movchan A, Movchan N, Jones I. Transformation elastodynamics and cloaking for flexural waves. J Mech Phys Solids 2014;72:131–43.
[27] Park J, Park C, Lee K, Lee S. Acoustic superlens using membrane-based metamaterials. Appl Phys Lett 2015;106(5):051901.
[28] Misseroni D, Colquitt D, Movchan A, Movchan N, Jones I. Cymatics for the cloaking of flexural vibrations in a structured plate. Sci Rep 2016;6:23929.
[29] Chen Y, Qian F, Zuo L, Scarpa F, Wang L. Broadband and multiband vibration mitigation in lattice metamaterials with sinusoidally-shaped ligaments. Extrem Mech Lett 2017;17:24–32.
[30] Bordiga G, Cabras L, Piccolroaz A, Bigoni D. Prestress tuning of negative refraction and wave channeling from flexural sources. Appl Phys Lett 2019;114:041901.
[31] Al-Ketan O, Rezgui R, Rowshan R, Du H, Fang NX, Abu Al-Rub RK. Microarchitected stretching-dominated mechanical metamaterials with minimal surface topologies. Adv Energy Mater 2018;20(9):1800029.
[32] Lim C, Li JT, Zhao Z, et al. Lightweight architected lattice phononic crystals with broadband and multiband vibration mitigation characteristics. Extrem Mech Lett 2020;41:100994.
[33] Lim C, et al. From photonic crystals to seismic metamaterials: A review via phononic crystals and acoustic metamaterials. Arch Comput Methods Eng 2021;1–62.
[34] Xue Y, Zhang X. Self-adaptive acoustic cloak enabled by soft mechanical metamaterials. Extrem Mech Lett 2021;46:101347.
[35] Diaz A, Haddow A, Ma L. Design of band-gap grid structures. Struct Multidiscip Optim 2005;29(6):418–31.
[36] Bacigalupo A, Lepidi M, Gnecco G, Gambarotta L. Optimal design of auxetic hexachiral metamaterials with local resonators. Smart Mater Struct 2016;25(5):054009.
[37] Ranjbar M, Boldrin L, Scarpa F, Neild S, Patsias S. Vibroacoustic optimization of anti-tetrachiral and auxetic hexagonal sandwich panels with gradient geometry. Smart Mater Struct 2016;25(5):054012.
[38] Wang ZP, Poh LH, Dirrenberger J, Zhu Y, Forest S. Isogeometric shape optimization of smoothed petal auxetic structures via computational periodic homogenization. Comput Methods Appl Mech Engrg 2017;323:250–71.
[39] Bacigalupo A, Gnecco G, Lepidi M, Gambarotta L. Machine-learning techniques for the optimal design of acoustic metamaterials. J Optim Theory Appl 2020;187(3):630–53.
[40] Bruggi M, Corigliano A. Optimal 2D auxetic micro-structures with band gap. Meccanica 2019;54(13):2001–27.
[41] Choi M, Oh M, Koo B, Cho S. Optimal design of lattice structures for controllable extremal band gaps. Sci Rep 2019;9(1):1–13.
[42] Kumar D, Wang Z, Poh LH, Quek ST. Isogeometric shape optimization of smoothed petal auxetics with prescribed nonlinear deformation. Comput Methods Appl Mech Engrg 2019;356:16–43.
[43] Rong J, Ye W. Topology optimization design scheme for broadband non-resonant hyperbolic elastic metamaterials. Comput Methods Appl Mech Engrg 2019;344:819–36.
[44] Thorp O, Ruzzene M, Baz A. Attenuation and localization of wave propagation in rods with periodic shunted piezoelectric patches. Smart Mater Struct 2001;10(5):979.
[45] Airoldi L, Ruzzene M. Design of tunable acoustic metamaterials through periodic arrays of resonant shunted piezos. New J Phys 2011;13(11):113010.
[46] Casadei F, Delpero T, Bergamini A, Ermanni P, Ruzzene M. Piezoelectric resonator arrays for tunable acoustic waveguides and metamaterials. J Appl Phys 2012;112(6):064902.
[47] Collet M, Ouisse M, Ichchou MN. Structural energy flow optimization through adaptive shunted piezoelectric metacomposites. J Intell Mater Syst Struct 2012;23(15):1661–77.
[48] Chen Y, Hu G, Huang G. An adaptive metamaterial beam with hybrid shunting circuits for extremely broadband control of flexural waves. Smart Mater Struct 2016;25(10):105036.
[49] Ouisse M, Collet M, Scarpa F. A piezo-shunted kirigami auxetic lattice for adaptive elastic wave filtering. Smart Mater Struct 2016;25(11):115016.
[50] Zhu R, Chen YY, Barnhart MV, Hu GK, Sun CT, Huang GL. Experimental study of an adaptive elastic metamaterial controlled by electric circuits. Appl Phys Lett 2016;108(1):011905.
[51] Xu J, Yan R, Tang J. Broadening bandgap width of piezoelectric metamaterial by introducing cavity. Appl Sci 2018;8(9):1606.
[52] Li G-H, Wang Y-Z, Wang Y-S. Active control on switchable waveguide of elastic wave metamaterials with the 3D printing technology. Sci Rep 2019;9(1):1–8.
[53] Bacigalupo A, De Bellis ML, Misseroni D. Design of tunable acoustic metamaterials with periodic piezoelectric microstructure. Extrem Mech Lett 2020;40:100977.
[54] Zhou W, Wu B, Chen Z, Chen W, Lim C, Reddy J. Actively controllable topological phase transition in homogeneous piezoelectric rod system. J Mech Phys Solids 2020;137:103824.
[55] Liu Y, Wang H, Fang W, Han Q, Liu D, Liang Y. Tunable control of subwavelength topological interface modes in locally resonance piezoelectric metamaterials. Compos Struct 2021;276:114541.
[56] Shechtman D, Blech I, Gratias D, Cahn JW. Metallic phase with long-range orientational order and no translational symmetry. Phys Rev Lett 1984;53(20):1951.
[57] Voronoi G. Nouvelles applications des paramètres continus à la théorie des formes quadratiques. Deuxième mémoire. Recherches sur les parallélloèdres primitifs.. J Reine Angew Math (Crelles J) 1908;1908(134):198–287.
[58] Penrose R. The role of aesthetics in pure and applied mathematical research. Bull Inst Math Appl 1974;10:266–71.
[59] Baake M, Grimm U. Further reading: Literature on quasicrystals. In: Quasicrystals. Springer; 2002, p. 539–44.
[60] Kohmoto M, Sutherland B, Tang C. Critical wave functions and a cantor-set spectrum of a one-dimensional quasicrystal model. Phys Rev B 1987;35(3):1020.
[61] Liu Z, Zhang W. Bifurcation in band-gap structures and extended states of piezoelectric thue-morse superlattices. Phys Rev B 2007;75(6):064207.
[62] Esaki K, Sato M, Kohmoto M. Wave propagation through cantor-set media: chaos, scaling, and fractal structures. Phys Rev E Stat Nonlinear Soft Matter Phys 2009;79(5 Pt 2):056226.
[63] Janot C. Quasicrystals: a primer. Oxford: Clarendon; 1994.
[64] Gei M. Wave propagation in quasiperiodic structures: stop/pass band distribution and prestress effects. Int J Solids Struct 2010;47(22–23):3067–75.
[65] Ning R, Liu S, Zhang H, Kong X, Bian B, Bao J. Wideband absorption in fibonacci quasi-periodic graphene-based hyperbolic metamaterials. J Opt 2014;16(12):125108.
[66] Ajlouni R, et al. Quasi-periodic geometry for architectural acoustics. Enquiry ARCC J Archit Res 2018;15(1):42–61.
[67] Ying Z, Ni Y, Huan R. Vibration response characteristics of quasi-periodic sandwich beam with magnetorheological visco-elastomer core under random support excitations. J Vib Acoust 2018;140(5).

[68] Glacet A, Tanguy A, Réthoré J. Vibrational properties of quasi-periodic beam structures. J Sound Vib 2019;442:624–44.
[69] Gei M, Chen Z, Bosi F, Morini L. Phononic canonical quasicrystalline waveguides. Appl Phys Lett 2020;116(24):241903.
[70] Timorian S, Ouisse M, Bouhaddi N, De Rosa S, Franco F. Numerical investigations and experimental measurements on the structural dynamic behaviour of quasi-periodic meta-materials. Mech Syst Signal Process 2020;136:106516.
[71] Wang Y, Sigmund O. Quasiperiodic mechanical metamaterials with extreme isotropic stiffness. Extrem Mech Lett 2020;34:100596.
[72] Toupin R. Stress tensors in elastic dielectrics. Arch Ration Mech Anal 1960;5(1):440–52.
[73] Bacigalupo A, Gambarotta L. Second-gradient homogenized model for wave propagation in heterogeneous periodic media. Int J Solids Struct 2014;51(5):1052–65.
[74] De Bellis ML, Bacigalupo A, Zavarise G. Characterization of hybrid piezoelectric nanogenerators through asymptotic homogenization. Comput Methods Appl Mech Engrg 2019;355:1148–86.
[75] Sun C-T, Achenbach JD, Herrmann G. Time-harmonic waves in a stratified medium propagating in the direction of the layering. J Appl Mech 1968;35:408–11.
[76] Lee HJ, Zhang S, Bar-Cohen Y, Sherrit S. High temperature, high power piezoelectric composite transducers. Sensors 2014;14(8):14526–52.
[77] Iyer S, Venkatesh T. Electromechanical response of (3–0,3–1) particulate, fibrous, and porous piezoelectric composites with anisotropic constituents: A model based on the homogenization method. Int J Solids Struct 2014;51(6):1221–34.